Chapter 14 – NUMERICAL SOLUTIONS FOR THE CAWAPI CONFIGURATION ON UNSTRUCTURED GRIDS AT UT-SIMCENTER, UNITED STATES

by

Steve L. Karman Jr., Brent Mitchell, Shane Sawyer, Justin Whitt

14.1 SUMMARY

Viscous solutions for a F-16XL configuration are computed using the CFD tools used by and developed at the University of Tennessee SimCenter at Chattanooga, Tennessee, USA. The study is performed in conjunction with a North Atlantic Treaty Organization Technical Team, AVT-113. Inviscid meshes are created using Gridgen. Viscous prismatic layers are added using a procedure that incorporates a Linear-Elastic smoothing scheme to perturb the existing mesh, creating room for the insertion of viscous layers. A vertex-centered, Reynolds averaged Navier-Stoke flow solver is used to compute seven test cases, defined by the NATO Technical Team AVT-113. Comparisons are made with available flight test data in the form of surface pressure coefficients.

14.2 INTRODUCTION

North Atlantic Treaty Organization (NATO) Technical Team AVT-113 was formed to investigate the state of the art in Computational Fluid Dynamics (CFD) solvers applied to viscous vortical flowfields. The goal of the study was to determine the accuracy and efficiency of modern CFD methods for analysis of highly vortical viscous flowfields typically encountered in modern fighter aircraft. The team is comprised of experimentalists and CFD researchers in the United States and Europe. The configuration chosen for the study is the F-16XL, originally built by General Dynamics. The only two existing F-16XL aircraft are owned by the National Air and Space Administration (NASA) in the United States and are used to conduct aerodynamic research. Data collected during flight tests includes surface pressures, boundary layer rakes and flow visualization [14-1]. This data can be used to validate the accuracy of CFD solvers. The NATO AVT-113 team selected a series of flight conditions to use in this CFD study. The flight conditions range from subsonic to transonic Mach numbers. The angle of attack range extends to near 19 degrees. These flight regimes generate multiple vortices that flow over the upper surface of the configuration and interact in numerous ways.

This chapter presents the results obtained at the University of Tennessee SimCenter at Chattanooga (UT SimCenter). The methods used by the UT SimCenter include some commercial CFD software packages, as well as some tools developed at the SimCenter. Brief descriptions of the procedures used in the analyses will be provided. The Navier-Stokes computations for seven cases are compared with data taken during the flight test.

14.3 UNSTRUCTURED MESH GENERATION

Two separate mesh generation programs were used to generate the viscous meshes for these analyses. The first program was a commercially available mesh generation package known as Gridgen [14-2]. Gridgen was used to create an inviscid unstructured mesh. The second mesh generation program was developed at the SimCenter and was used to insert viscous layers in the inviscid mesh. Brief descriptions of the tools are described below.

14.3.1 Geometry

The NATO Technical Team AVT-113 provided the F-16XL geometry in the form of an IGES file. Lockheed Martin Aeronautics Company produced the original IGES file. Some initial cleanup work was performed by NASA Langley Research Center to eliminate known gaps and overlaps in the defined surfaces. Additional cleanup work and geometry simplification was performed by EADS-M to prepare the geometry for mesh generation and analysis by all AVT-113 team members. Some of the simplifications included the elimination of duplicate geometry entities in regions such as the engine inlet lip and the elimination of the gap between the engine nozzle and the clamshell airbrake.

All major geometric features were defined in the final IGES file. The features included the air data probe at the nose, the cockpit canopy, the engine inlet and nozzle, the wing and vertical tail, the actuator pods and air dam on the wing and the wing tip rail and AIM-9 missile. The inlet duct was modeled all the way up to the compressor face. The nozzle duct was modeled from the turbine face aft. Also modeled was the boundary layer diverter located between the inlet and the fuselage.

14.3.2 Inviscid Mesh

Gridgen was used to create an unstructured inviscid mesh, comprised of mostly tetrahedra [14-2]. Surface meshes, consisting of triangular elements, were created on the geometry defined by the IGES file. Care was taken to ensure proper resolution of pertinent geometric features such as the leading and trailing edge of the wing. The high curvature of the leading and trailing edges needed fine resolution in the chord-wise direction to resolve the shape. The unstructured triangular surface meshing in Gridgen imposes nearly isometric triangular elements. In order to provide the desired resolution in the chord-wise direction and not have an excessive number of triangular elements in the span-wise direction a structured grid was used along sections of the leading and trailing edges of the wing. The aspect ratio of the quadrilateral elements was imposed to be no larger than 15. The resulting structured quadrilateral surface mesh was then converted to an unstructured triangular mesh by subdividing the quadrilateral elements into two triangles. Figure 14-1 shows a section of the leading edge where the converted structured mesh domain meets the unstructured mesh domains. A view of the mesh on the symmetry plane is shown in Figure 14-2.

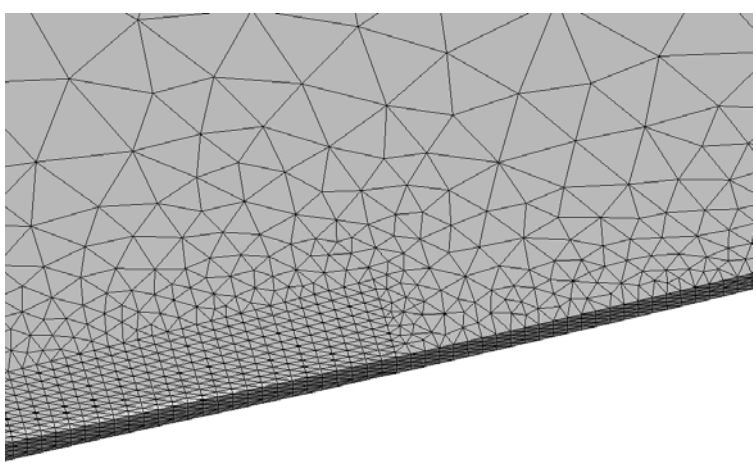

Figure 14-1: Leading Edge Mesh Showing the Converted Structured Domain Next to an Unstructured Domain.

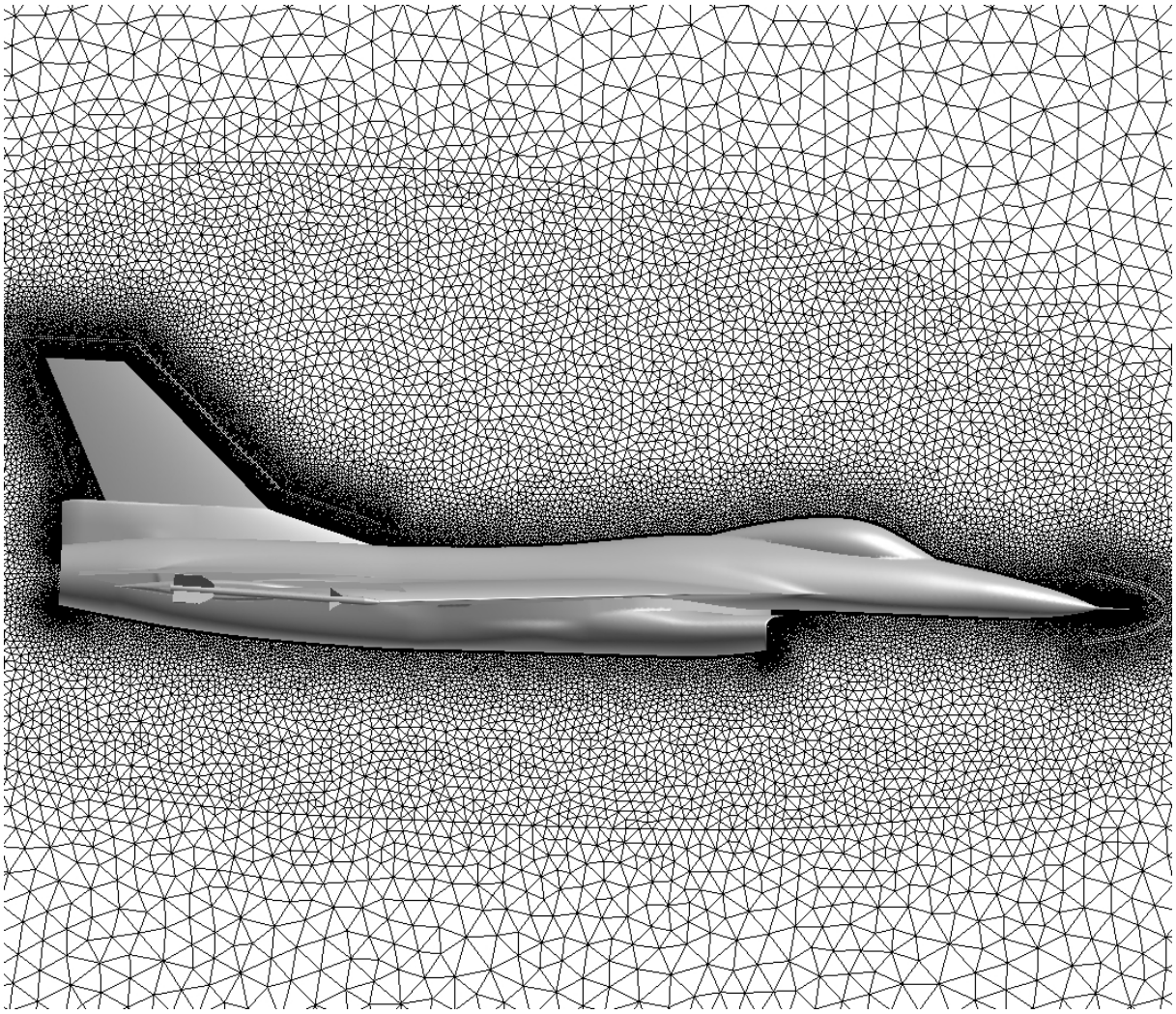

Figure 14-2: Symmetry Plane Mesh.

Baffle surfaces were used to control the spacing of the volume mesh, resulting in a hybrid unstructured inviscid mesh. The quadrilateral elements shown in the figure around the nose and tail are a result of these baffles. Additional baffles were created around the leading edge and trailing edge of the wing and at a near field boundary within a body length of the aircraft. The near field baffle boundaries can also be seen in Figure 14-2.

Views of the upper and lower surface mesh are shown in Figure 14-3. The total number of surface elements for the aircraft, minus the inlet face and nozzle face, is 599,676. The final inviscid mesh contained 4,858,525 nodes, 27,701,876 tetrahedra, 2186 pyramid and 195,044 prisms.

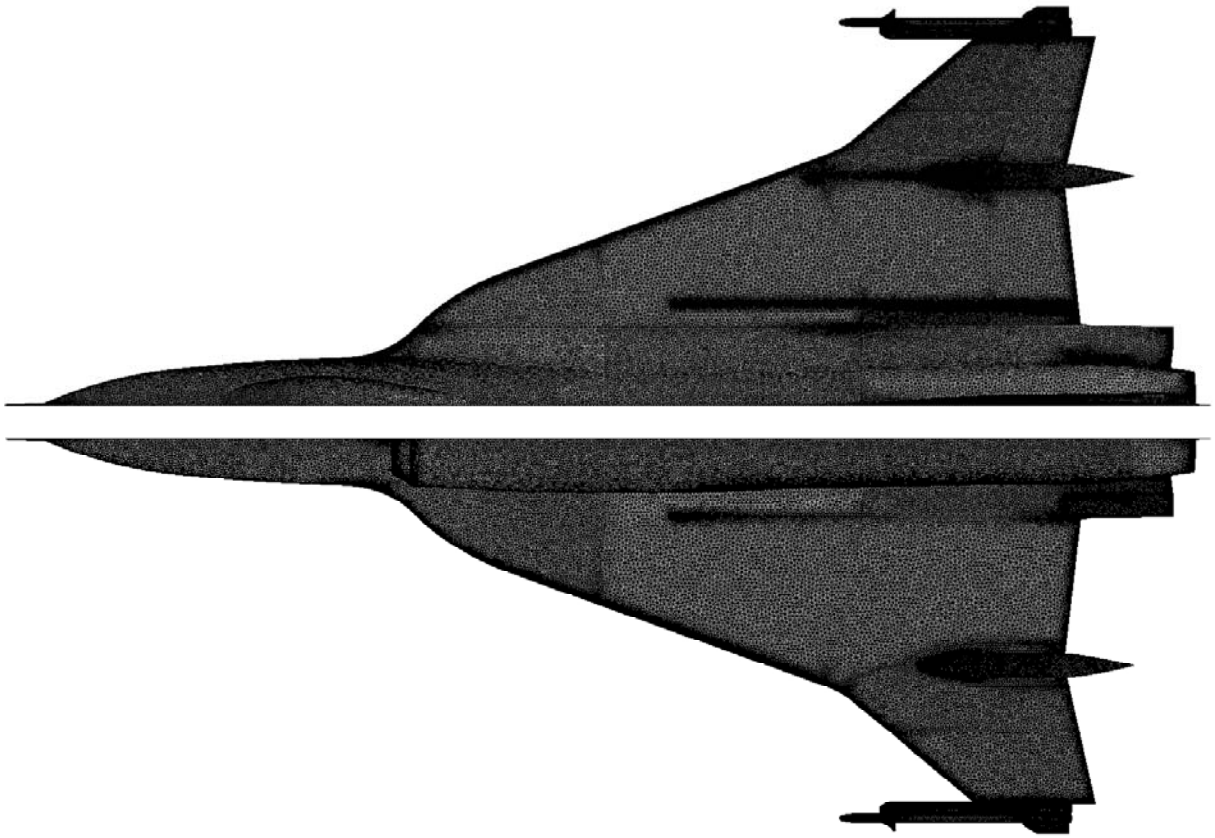

Figure 14-3: Top and Bottom Views of the Surface Mesh.

14.3.3 Viscous Mesh

A second mesh generation program was used to insert layers of triangular prismatic elements at the no-slip surfaces of the geometry [14-3]. This method uses a Linear-Elastic mesh-smoothing scheme to push the existing mesh away from the surface, making room for the viscous elements. The term normally used to define Young's Modulus in the linear-elastic relations is defined using a combination of element aspect ratio and corner angles to provide stiffness in regions of tight grid spacing. The Poisson's ratio term was set to a constant of 0.25. Only one layer of points is added at a time in reverse order; the top layer is added first and the final layer near the wall is added last. Points are only added where the local mesh spacing is larger than the desired spacing for the current layer. As a result, the number of triangular prismatic elements in a column varies over the surface. Figure 14-4 and Figure 14-5 show the varying number of elements per column for the mesh at the inlet. This capability allows the outer layer of prisms to match the spacing of the local tetrahedral elements without forcing each column to have unnecessary layers, which could result in kinking or buckling of the outer viscous layers.

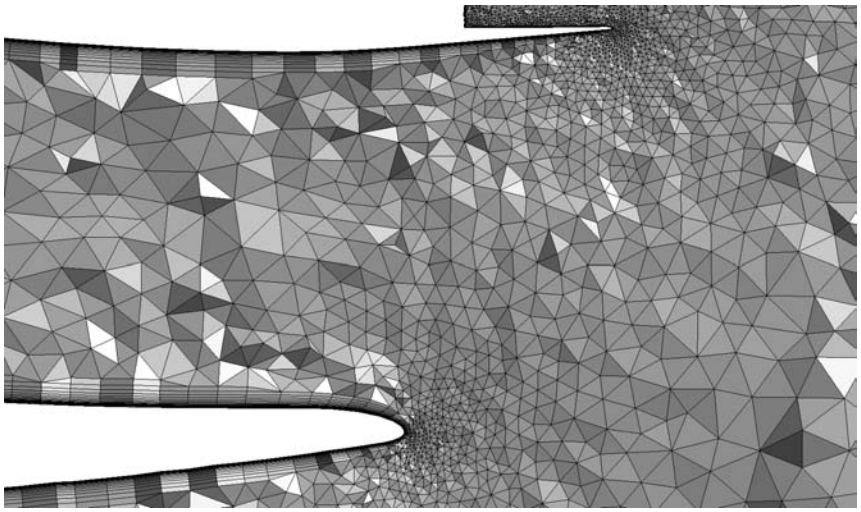

Figure 14-4: Crinkle Cut of Mesh Near the Symmetry Plane at the Inlet.

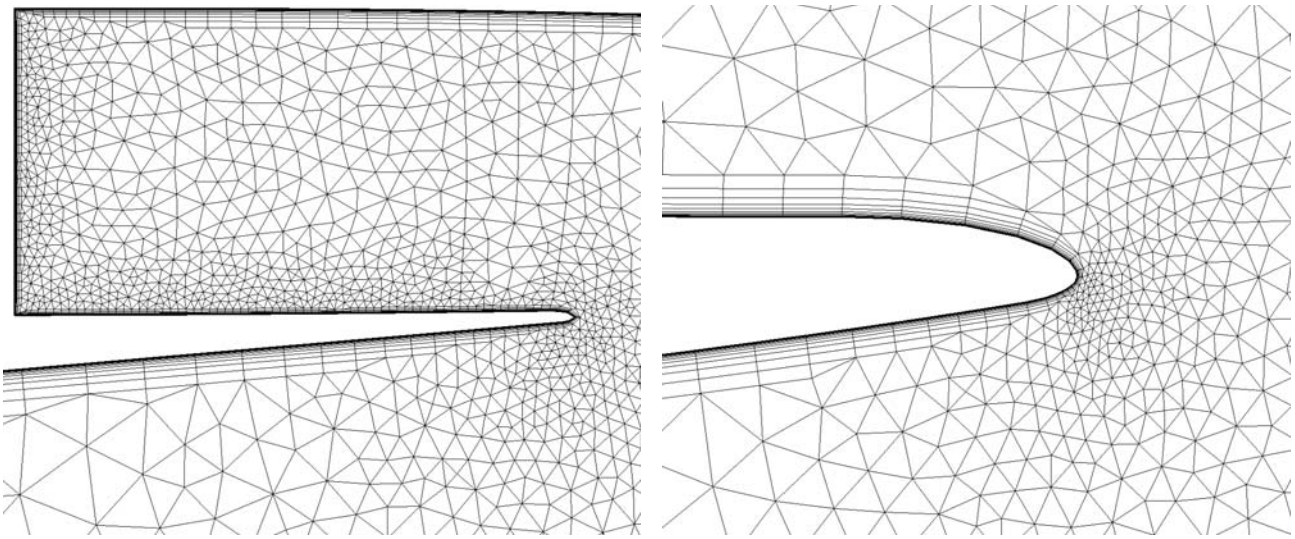

Figure 14-5: Magnified Views of Symmetry Plane Mesh at the Upper Inlet Lip (left) and the Lower Inlet Lip (right).

A total of 25 layers were requested for the viscous region. The initial spacing was specified to correspond to an estimated Y+ value of 1. The height of the subsequent layers increases according to a geometric progression factor of 1.15 and a geometric growth rate of 1.02. A view of the viscous layers for the tip missile fins is shown in Figure 14-6. Finer resolution tetrahedra can be seen in the gap region between the fine and the missile rail. The layer insertion strategy matched the normal spacing of the layers with the existing local tetrahedral mesh. The half-model, viscous mesh contained 10,586,377 nodes, 28,092,773 tetrahedra, 982,975 pyramid and 10,822,176 prisms.

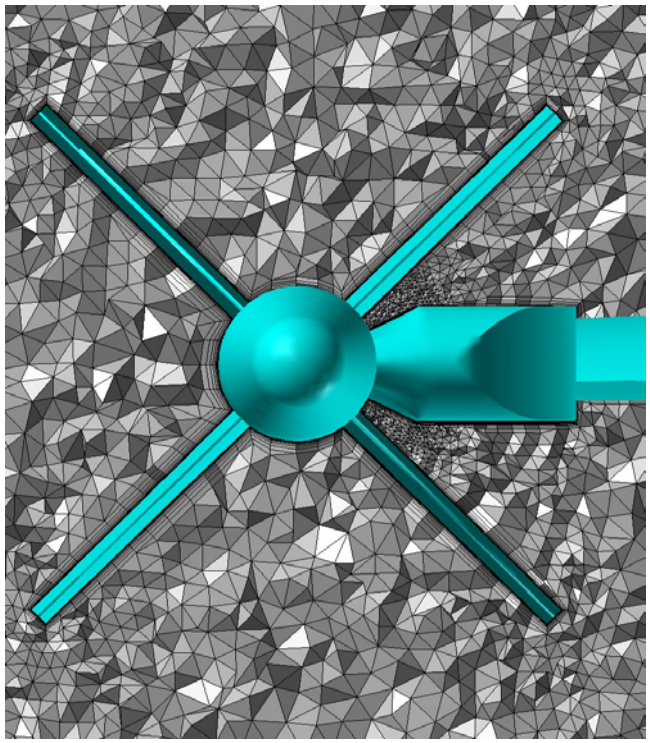

Figure 14-6: Magnified View of Axial Cut Through Tip Missile Fins and Wing.

14.4 UNSTRUCTURED FLOW SOLVER

The present flowfield solution algorithm used at the UT-SimCenter is related to several previous efforts and has evolved over more than 15 years of development. The approach is an evolution of the implicit flow solver and code of Anderson et al. [14-5] [14-6] [14-6]. The solver developed in this series of works demonstrated 3D, implicit, high Reynolds number solution capability. Aspects of the present approach are also related to the parallel multi-block structured grid solver of Pankajakshan [14-7]. The parallel version of the unstructured algorithm is detailed in Reference [14-8]. Brief descriptions of some of the aspects of the flow solver are described below.

14.4.1 Arbitrary Mach Algorithm

The staple of the structured and unstructured SimCenter flow solution code is an algorithm well suited for simulation of both high-speed and low-speed flows. This formulation was presented by Briley and is termed the arbitrary Mach number algorithm, which is a preconditioned Roe flux-difference formulation for non-dimensional primitive variables [14-9]. The unsteady three-dimensional compressible Reynolds-averaged Navier-Stokes equations are presented here in Cartesian coordinates and in conservative form:

$$\frac{\partial}{\partial t}\int_{\Omega} Q dV + \int_{\partial\Omega} \vec{F} \bullet \hat{n} dA = \frac{M_\infty}{\mathrm{Re}} \int_{\partial\Omega} \vec{G} \bullet \hat{n} dA \qquad (1)$$

The solution variables are expressed in their primitive form in the arbitrary Mach number algorithm:

$$Q = [\rho, u, v, w, P]^T \tag{2}$$

The arbitrary Mach algorithm depends on a simple, single-parameter diagonal matrix for conditioning of the system matrix eigenvalues:

$$\Gamma = \text{diag}\begin{bmatrix}1 & 1 & 1 & 1 & \beta\end{bmatrix} \tag{3}$$

where β is M_r^2 (reference Mach number) unless $M_r > 1$, in which case β = 1. This leads to a low-cost implementation of the algorithm that is an effective convergence accelerator that converges favorably regardless of the local flow speed. Thus, simulation domains that contain regions of high-speed and low-speed flow are particularly well treated by this algorithm. The algorithmic approach has been validated for a range of problems, from simple to complex geometries and from low (M = 0.001, incompressible) to high (supersonic) speed flows [14-9]. Above M = 1, this algorithm behaves exactly as a conservative compressible flow solver with solution variables in the primitive form. A flux limiter was employed to handle strong discontinuities and prevent overshoots in flow variables.

14.4.2 Iteration Hierarchy

The time evolution algorithm uses Newton iterations to remove time linearization error in the unsteady terms. The time evolution algorithm is implicit, such that a linear system of equations is solved at each Newton iteration. The solution of the linear system is obtained via a Symmetric Gauss Seidel algorithm (point relaxation) that has been used successfully and extensively [14-8].

14.4.3 Parallel Solver

The parallel solution procedure consists of a scalable solution algorithm implemented to run efficiently on grid sub-domains distributed across multiple processes and communicating through MPI. The algorithm has multiple nested kernels viz. time step, Newton iteration, LU/SGS iteration etc., and the sub-domain coupling is at the innermost level, i.e., in the solution of the linear system. A block-Jacobi type updating of the sub-domain boundaries ensures efficient parallelization with a small incremental cost incurred in terms of sub-iterations required to recover the convergence rate of the sequential algorithm. The solutions obtained in this study were partitioned over as few as 48 and as many as 200 processors. The full model solutions used 200 processors.

14.4.4 Turbulence Modeling

The current SimCenter flow solvers have a wide range of turbulence models including the one equation Spalart-Almaras and Menter-SAS models, the two equation q-ω and k-ε/k-ω models. The Spalart-Almaras turbulence model was initially used in this study. After a brief numerical study for the first test case comparing the results from using the various turbulence models, the two equations q-ω and k-ε/k-ω model was selected for use in the remaining cases in this study.

14.5 FLIGHT CONDITIONS AND ENGINE PARAMETERS

The details of the Flight Conditions (FC) of interest are given in Table 14-1 and the associated engine conditions are given in Table 14-2. These cover a range of Mach numbers from subsonic to transonic, angles of attack, α, up to ~20°, sideslips, β, ranging from ~-5° to ~5°, and Reynolds numbers up to ~89 million. For actual values of β < 1°, the computations were made at a β_{nom} = 0°. The first four FCs listed were those that all participants agreed to compute for comparison with the published results [14-1]. The other three were added to facilitate

comparisons either at a higher value of α or at the actual β value, nominally ±5°. Of course, solutions at these larger β values require full configuration modeling.

Table 14-1: Seven Flight Conditions Examined

Flight Condition	Actual Mach No.	Actual α	Actual β	Actual Reynolds No.
FC7	0.304	11.89	-0.133	44.4E+06
FC19	0.36	11.85	+0.612	46.8E+06
FC46	0.527	10.4	+0.684	46.9E+06
FC70	0.97	4.37	+0.310	88.77E+06
FC25	0.242	19.84	0.725	32.22E+06
FC50	0.434	13.56	+5.31	39.41E+06
FC51	0.441	12.89	-4.58	38.95E+06

Table 14-2: Associated Engine Parameters* for these Flight Conditions

Flight Condition	Free Stream Altitude, ft.	Free Stream Mach	Inlet Duct Exit Static Temp., degs. R	Inlet Duct Exit Static Press., psia	Inlet Duct Exit Velocity, ft/sec	Inlet Duct Exit Mach	Mixing Plane Total Temp., degs. R	Mixing Plane Total Press., psia
FC7	5000	0.304	498	11	379.6	0.347	1050	23
FC19	10000	0.36	485.8	10.2	345.8	0.32	1050	21.5
FC46	24000	0.527	443.6	5.85	404.3	0.39	1045	14.8
FC70	22300	0.97	519	10.65	464.7	0.416	1200	30
FC25	10000	0.242	470.1	8.72	474.8	0.447	1209	26.3
FC50	24000	0.434	440	5.16	483.3	0.47	1154	16.95
FC51	24000	0.441	431.8	5.19	468.6	0.46	1146	16.74

* The numbers in this table do not represent any particular engine.

14.6 RESULTS

Solutions for the four required cases and three optional cases are presented in this section. The results are compared with surface pressure coefficient data, when available. All three-dimensional flowfield images in this paper were created using Fieldview [14-10]. All two-dimensional plots were created using Tecplot 360 [14-11].

14.6.1 Adapted Mesh

Solutions for many of the flight conditions were computed on the viscous mesh described in Section 14.3.3 Comparisons with the available flight test data were made with mostly very good results. However, in many of the cases the comparisons at the outboard span stations did not agree well with the data. The suction peaks were too close to the wing leading edge. Various turbulence models were used to determine if the physical modeling had an effect on the result. The pressure coefficient comparison for 4 different turbulence-modeling options is shown in Figure 14-7. The case labeled Turb 1 used the Spalart-Allmaras turbulence model. The case labeled Turb 2 used the one equation Menter SAS model. Turb 5 is a two-equation, q-ω, k-ε/k-ω model hybrid. And Turb 5 DES combines the two equation model with a Detached Eddy Simulation model, requiring unsteady flowfield analysis. No significant improvement was observed with any of the turbulence models. It appeared as though the vortex was traveling more outboard than the data showed, so the mesh resolution in the outboard region was examined.

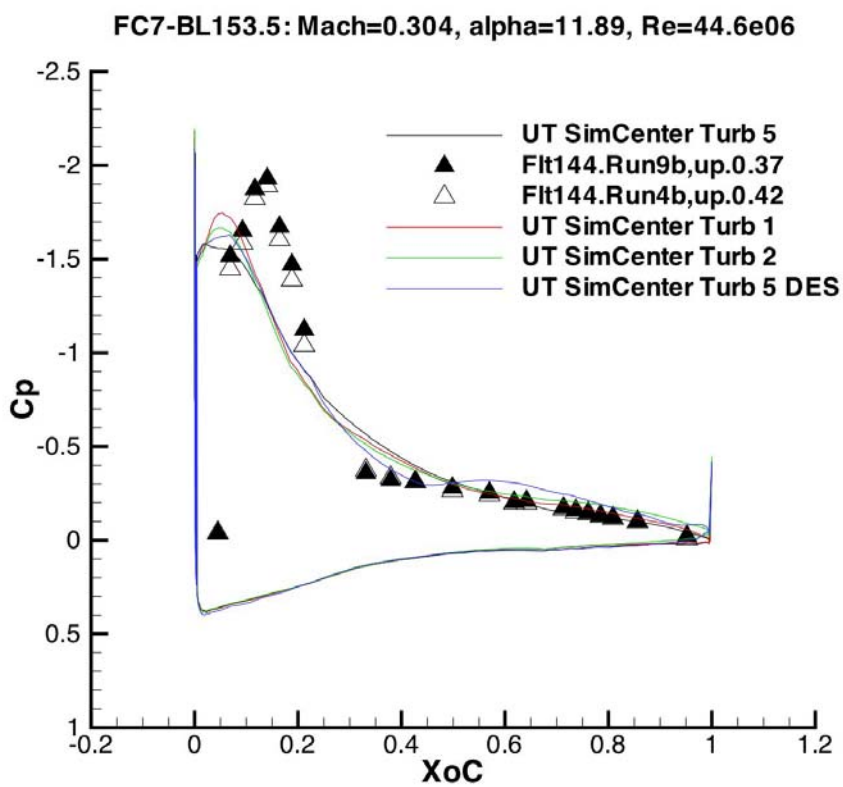

Figure 14-7: Various Turbulence Modeling Options did not Significantly Improve the Comparison at the Outboard Span Station.

A new mesh was created that increased the resolution in the vicinity of the expected trajectory of the vortex. This mesh adaptation was performed manually within the described meshing process and did not involve any solution-based mesh refinement. The original mesh and new mesh for the top wing surface at the outboard stations can be seen in Figure 14-8 and Figure 14-9, respectively. The increased resolution is readily apparent in the image of the new mesh. This mesh was subsequently used with the two-equation turbulence model to re-compute all flight conditions. All results presented below used this enhanced mesh in the calculations. The new half-model, viscous mesh contained 13,906,708 points, 32,395,936 tetrahedra, 166,230 pyramid, 15,770,674 prisms and 352,656 hexahedra. One mesh was used for all cases analyzed in this study. Mirror-copying the half-model mesh about the symmetry plane created the mesh for the full configuration cases. Time and resource limitations prevented a grid convergence study.

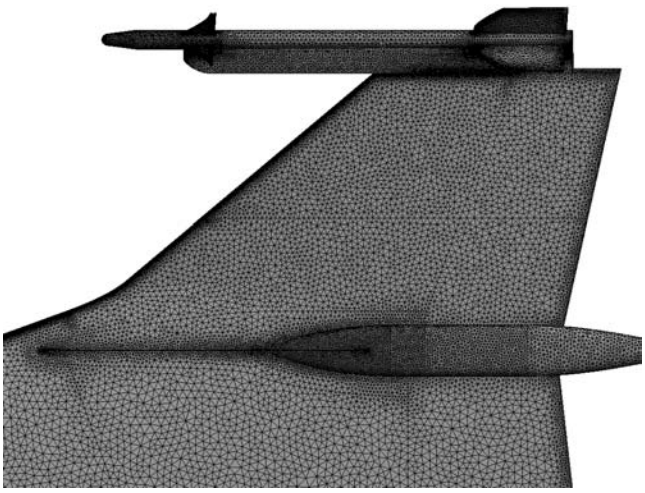

Figure 14-8: Top View of Original Surface Mesh at Outboard Wing Section.

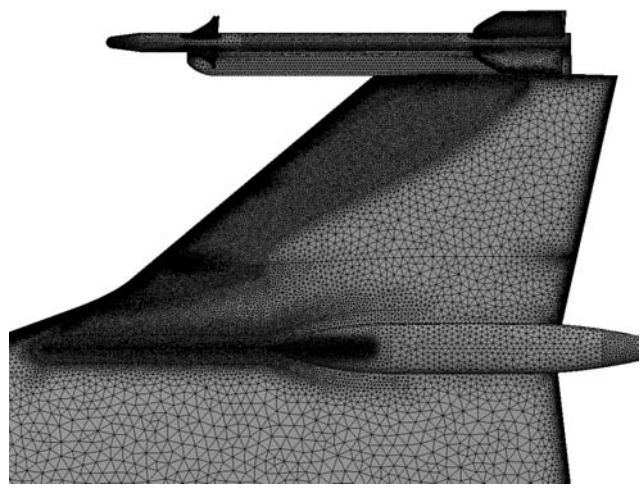

Figure 14-9: Top View of Adapted Surface Mesh at Outboard Wing Section.

14.6.2 Surface Pressure Coefficient Comparisons for All Flight Conditions

Surface pressure coefficient comparisons for span-wise stations and axial stations for all flight conditions are shown in Figure 14-10 through Figure 14-23. Each figure includes an image of the aircraft in the top of the figure to show the physical location of the various span stations or axial stations. The computed CFD solutions using the UT SimCenter solver are shown in solid lines. The flight test data is shown as filled and unfilled triangular symbols. The horizontal axes on the plots are normalized axial coordinate, X/C, from the leading edge for the span-wise station plots and normalized span-wise coordinate, Y/C, for the axial station plots. The vertical axes are the negative pressure coefficient. Some observations are provided in the following paragraphs.

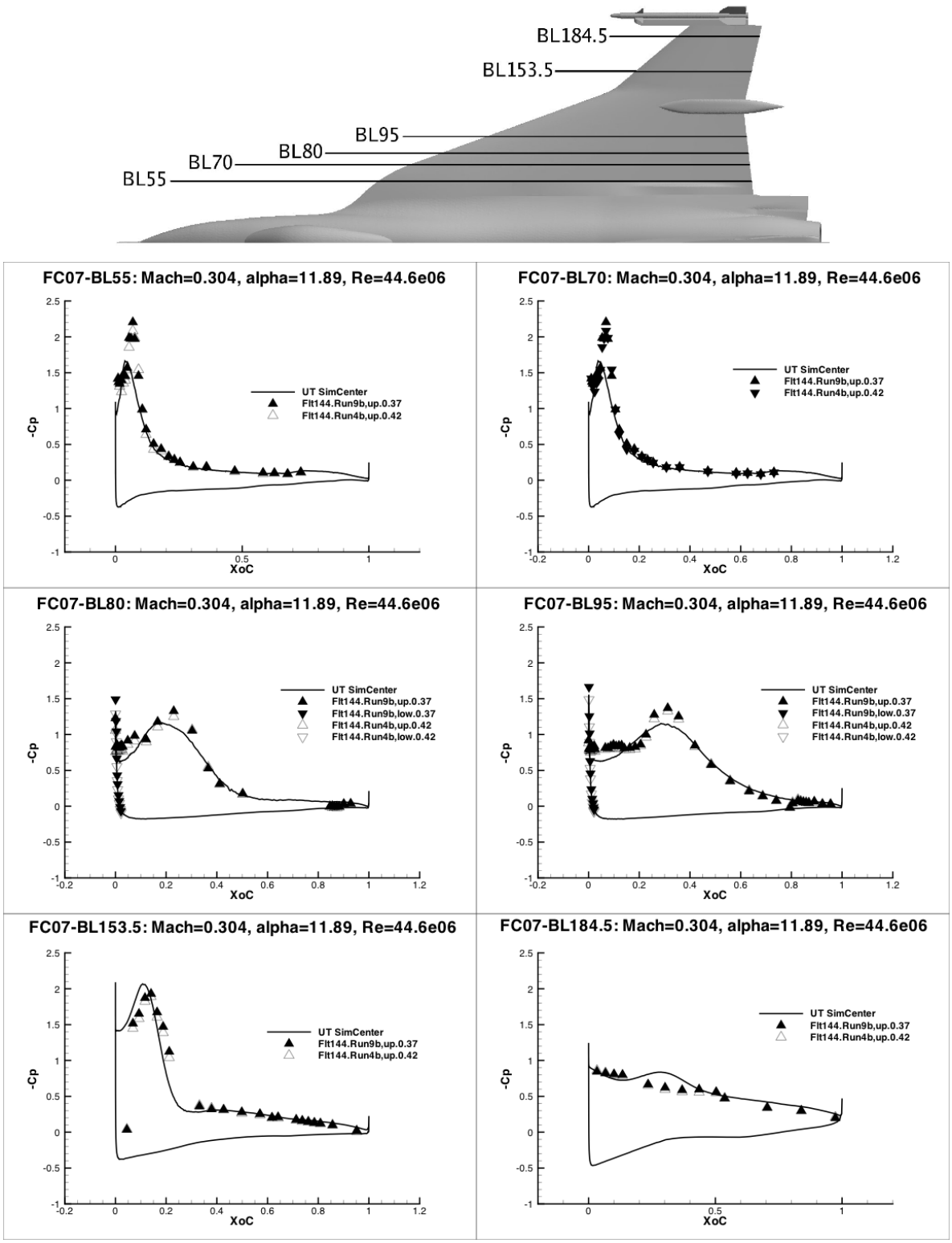

Figure 14-10: FC7 Surface Pressure Coefficient Comparisons for Span-Wise Stations.

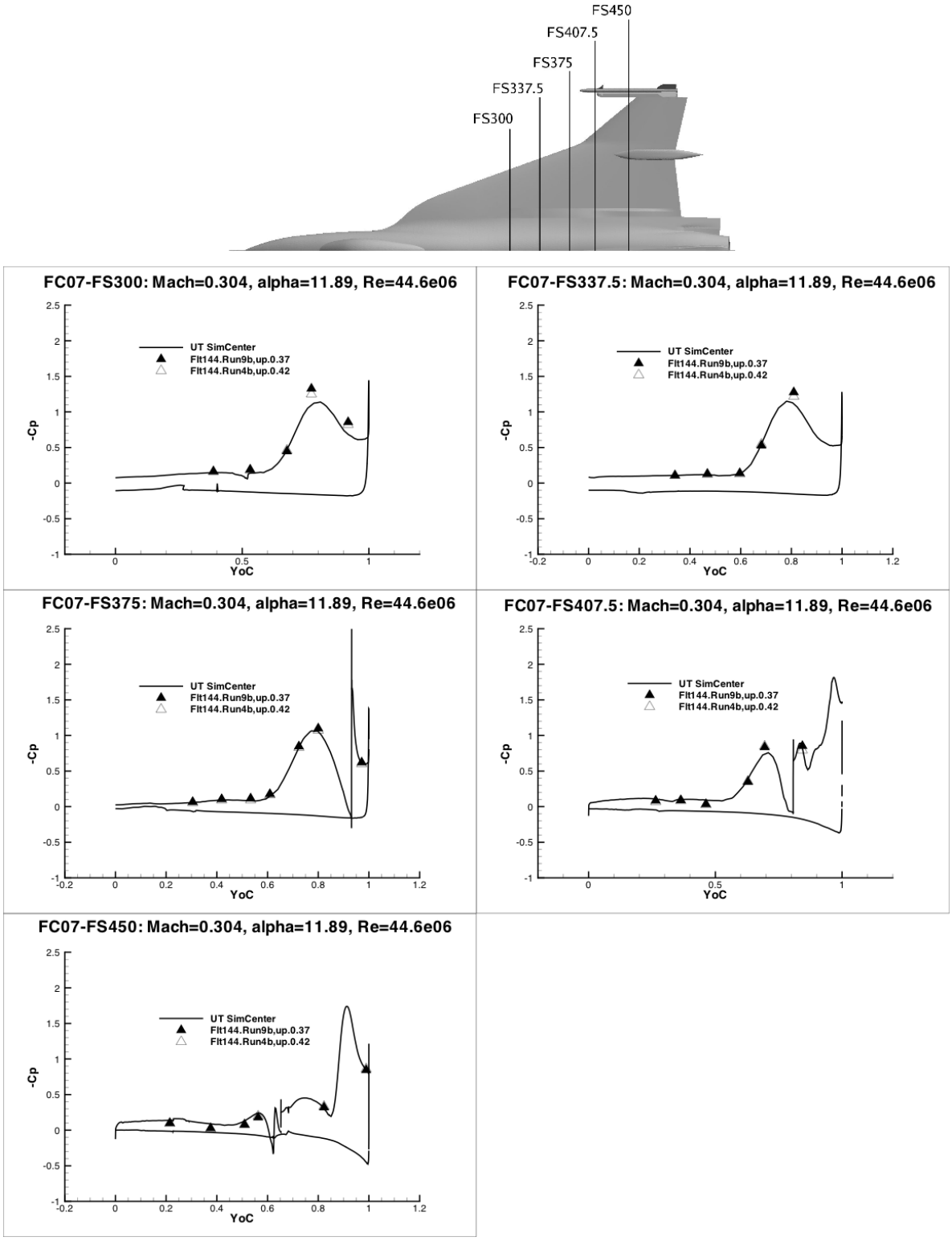

Figure 14-11: FC7 Surface Pressure Coefficient Comparisons for Axial Stations.

The comparisons for flight condition 7 (FC7) show good agreement with the flight test data. A couple of noticeable discrepancies occur at the suction peak of the two inboard stations, BL55 and BL70, and the suction peak at station BL153.5. The computed suction peaks are a little lower and positioned forward, slightly. Flight condition 19 (FC19) is compared to the same flight test data in Figure 14-12 and Figure 14-13. The freestream conditions are very close for these two cases; Mach 0.304 and alpha of 11.89 for FC7 and Mach 0.36 and alpha of 11.85 for FC19. The flight test data is reportedly at a Mach number of 0.37 and an angle of attack of 13 degrees. This could explain the slightly better agreement obtained with FC19.

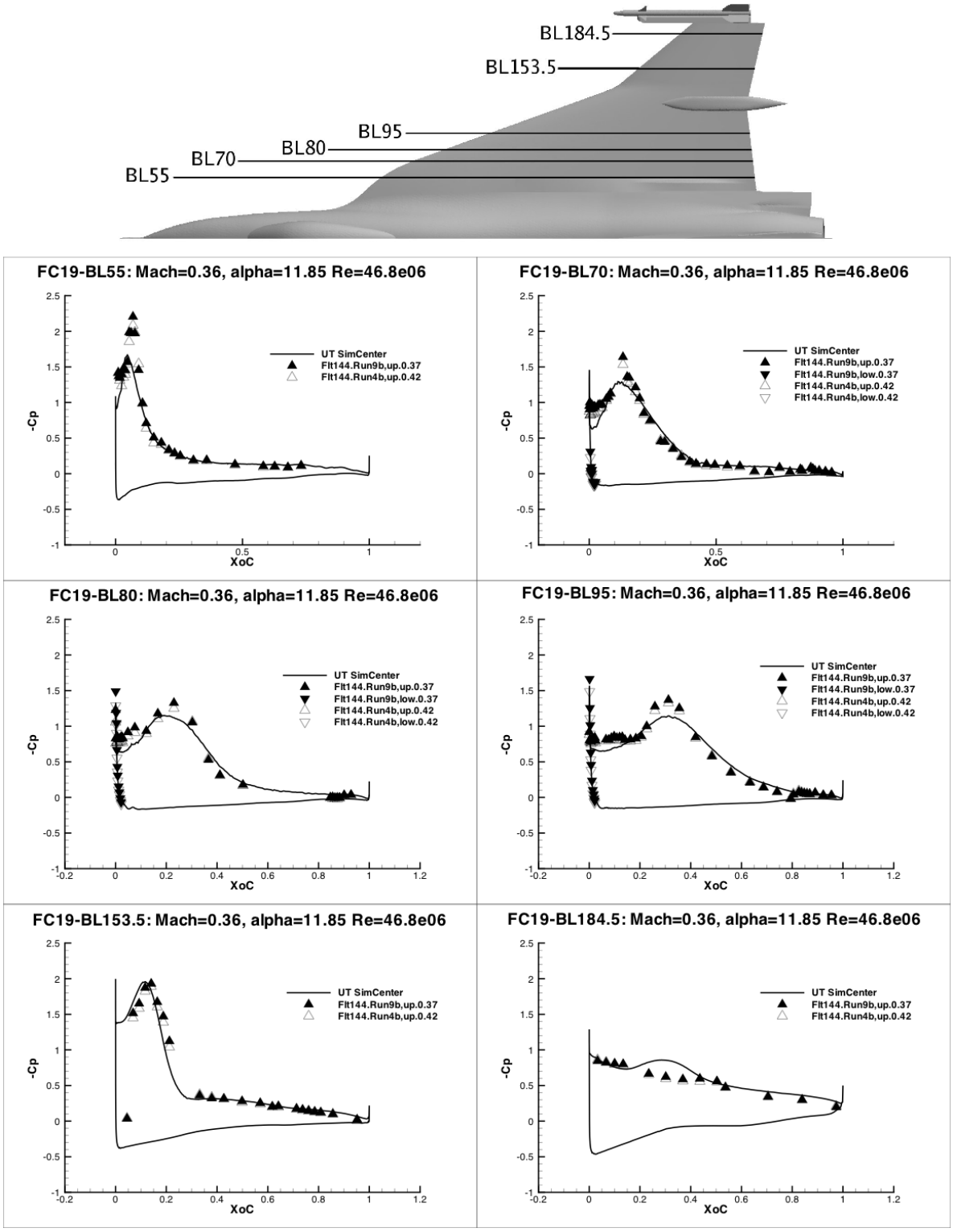

Figure 14-12: FC19 Surface Pressure Coefficient Comparisons for Span-Wise Stations.

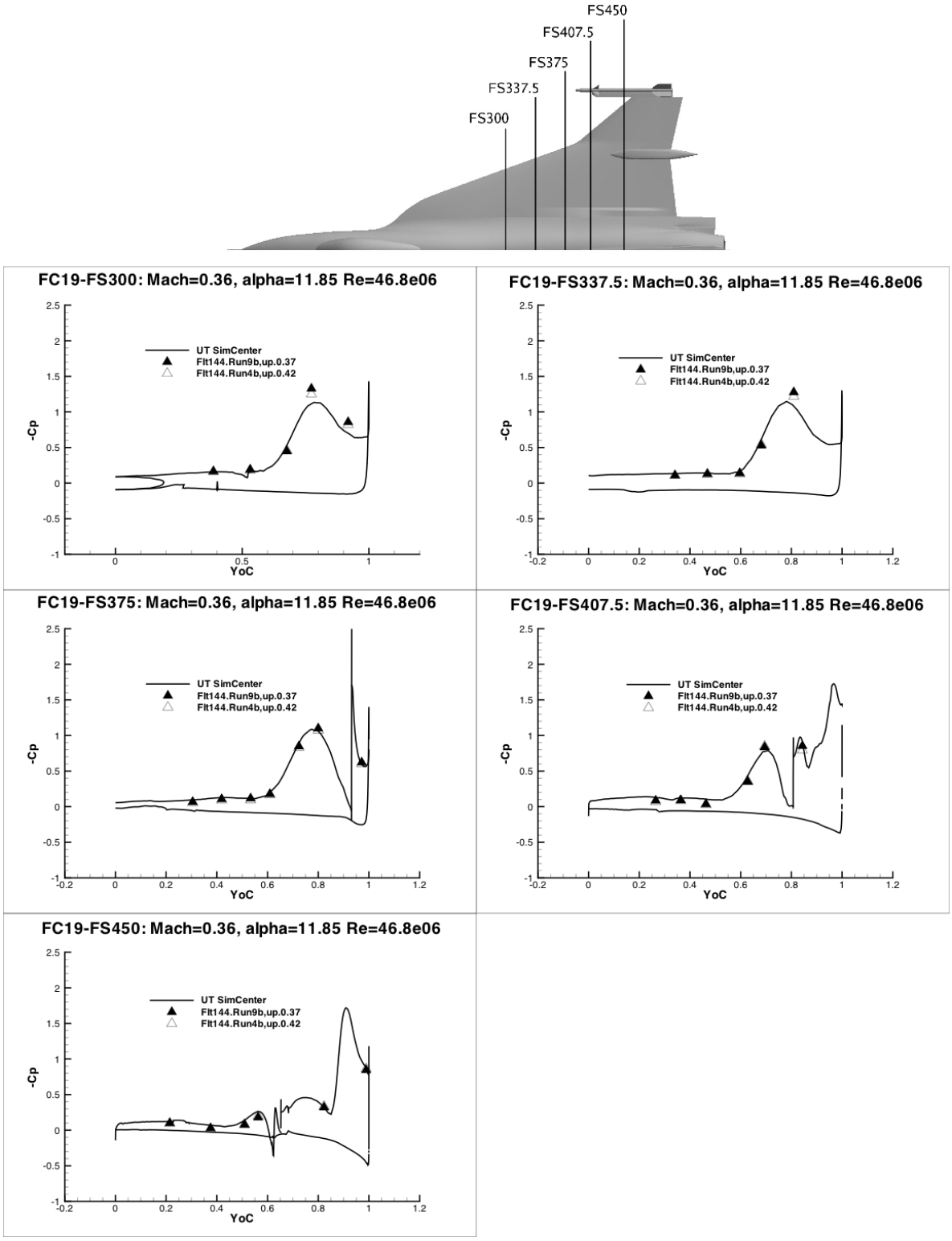

Figure 14-13: FC19 Surface Pressure Coefficient Comparisons for Axial Stations.

The comparisons for flight condition 46 (FC46), in Figure 14-14 and Figure 14-15 also show good agreement with the flight-test data; though span station 153.5 seems to show some differences between the computed solution and flight test results. The computed suction peak is slightly aft of the location in the flight-test data and is spread out more. The computed solution seems to show a larger (wider) vortex in this location. This is the first span station outboard of the air dam and was the focus of mesh adaptation mentioned in Section 14.6.1. It would seem from this plot that the adaptation caused the flow solver and turbulence model to over-compensate and spread the vortex out more. Although, this conjecture is not supported by the comparisons shown in the first two flight conditions or in other cases shown later.

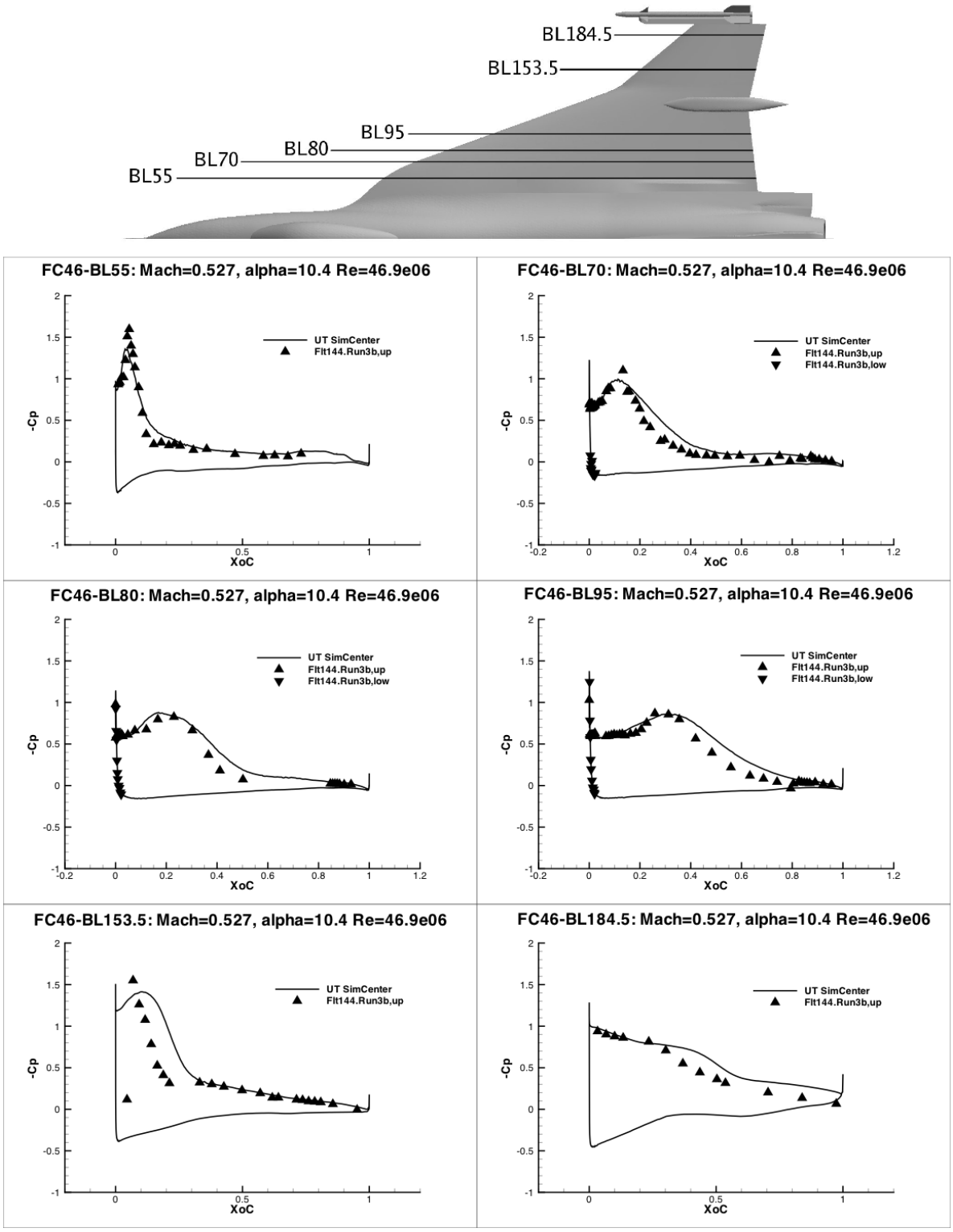

Figure 14-14: FC46 Surface Pressure Coefficient Comparisons for Span-Wise Stations.

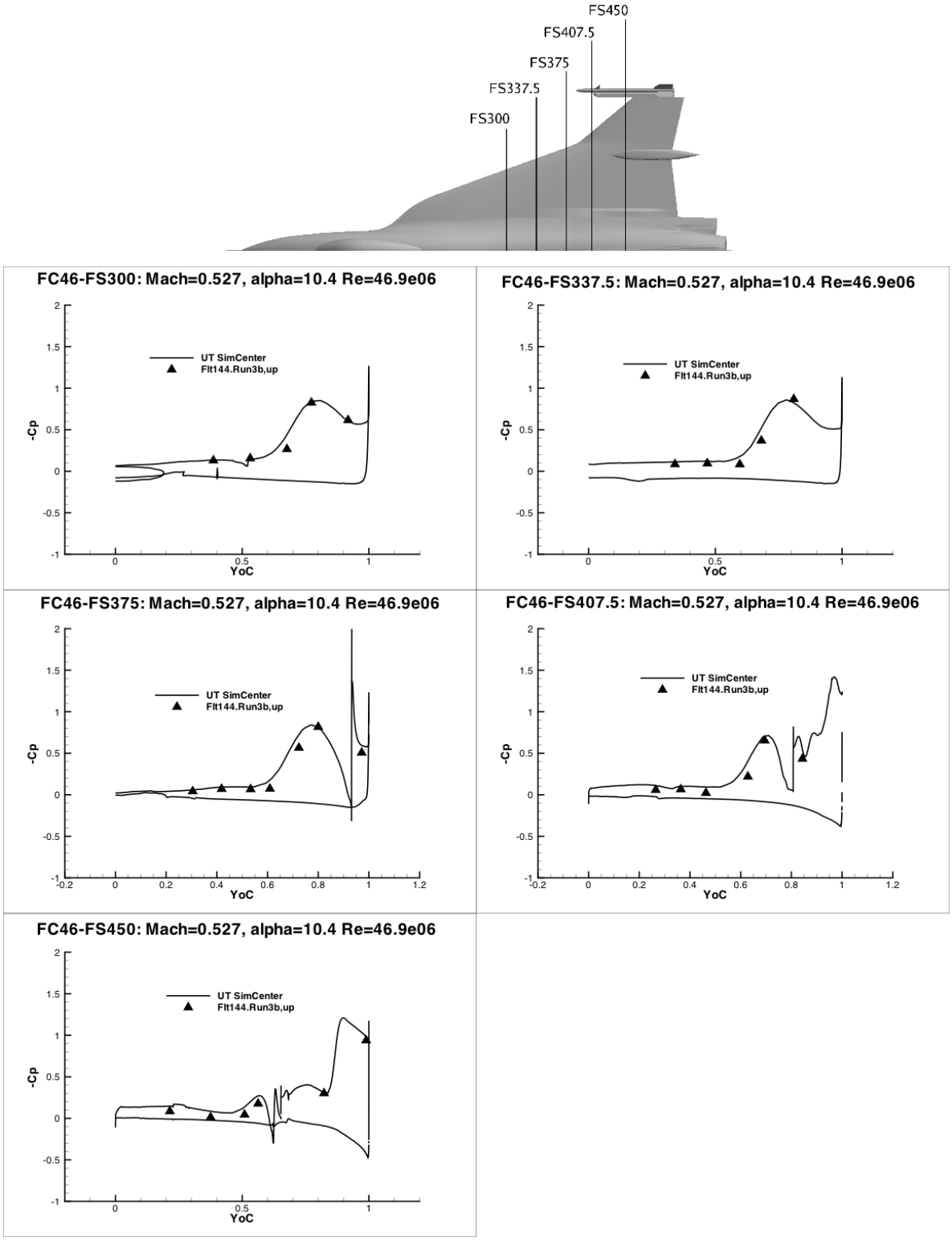

Figure 14-15: FC46 Surface Pressure Coefficient Comparisons for Axial Stations.

Comparisons for flight condition 70 (FC70), Figure 14-16 and Figure 14-17, show good agreement at span stations BL55 and BL95 and poor agreement elsewhere. After the case was computed, it was learned that the aircraft flight control system schedules the outboard leading edge flap between 5 and 9 degrees upward and the trailing edge flap about 2 degrees downward [14-1]. The geometry used to create the CFD model did not include leading or trailing edge flap deflections. The leading edge deflection could definitely impact the pressure distribution for the outboard stations. Lamar et al. in Reference [14-1] indicate that the small trailing edge deflection could also impact the pressure distribution and the shock location. So the differences at the two most outboard stations could be explained by neglecting to model the flap deflections. The differences at stations BL70 and BL80 cannot be explained by the flap deflections. From examining the flight test data between BL55 and BL95 it is hard to understand what physically takes place. These discrepancies also show up in the axial station plots for FS300, FS337.5 and FS375.

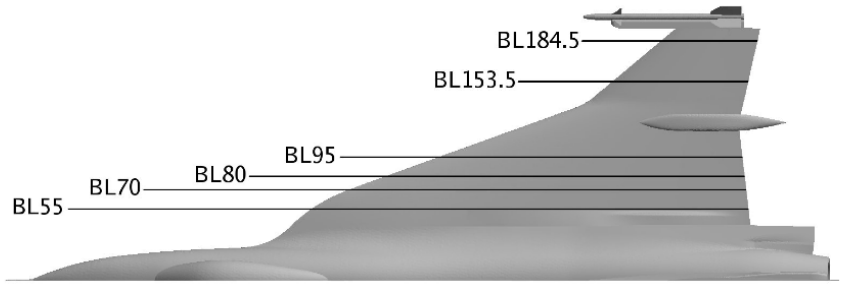

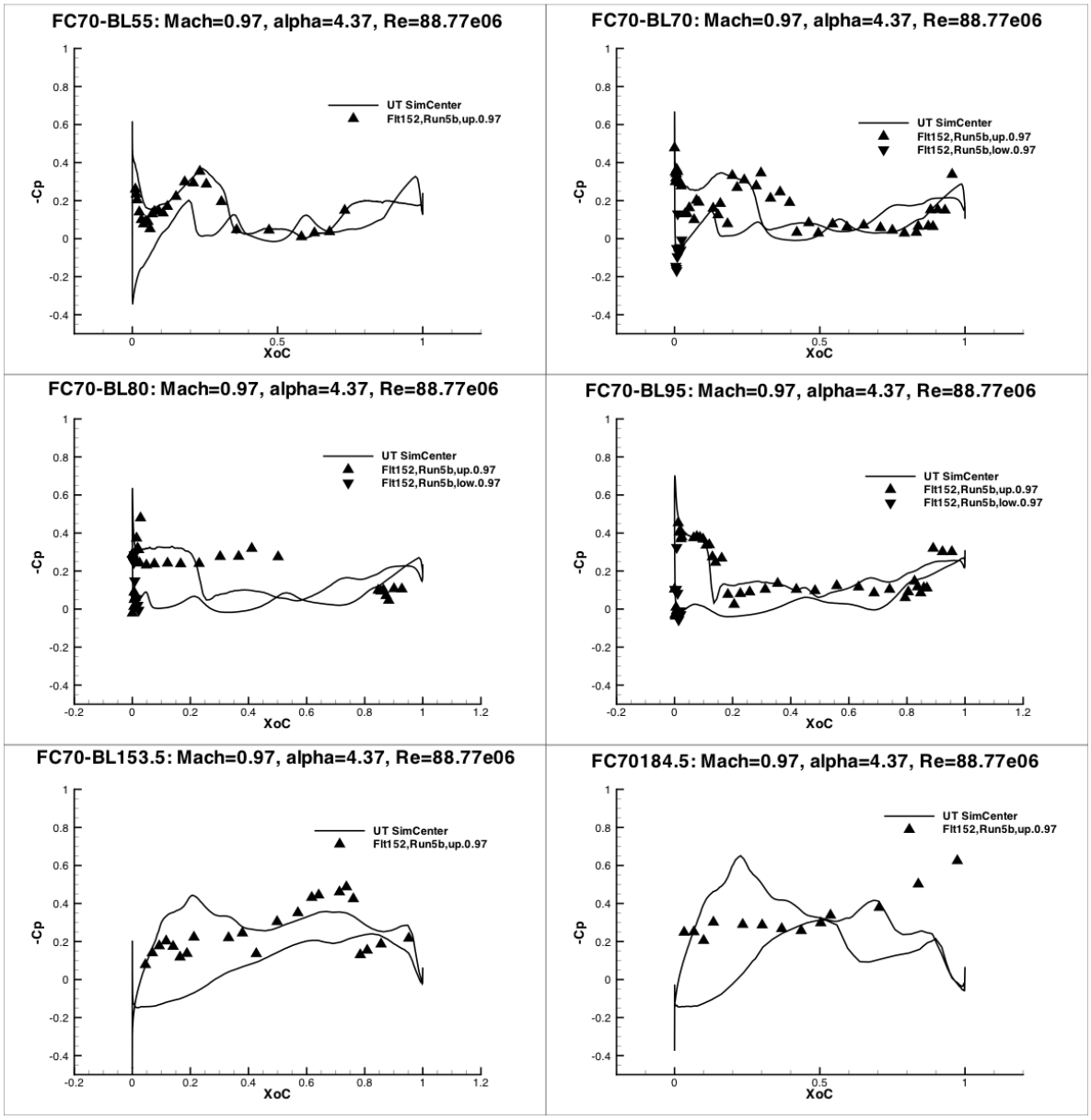

Figure 14-16: FC70 Surface Pressure Coefficient Comparisons for Span-Wise Stations.

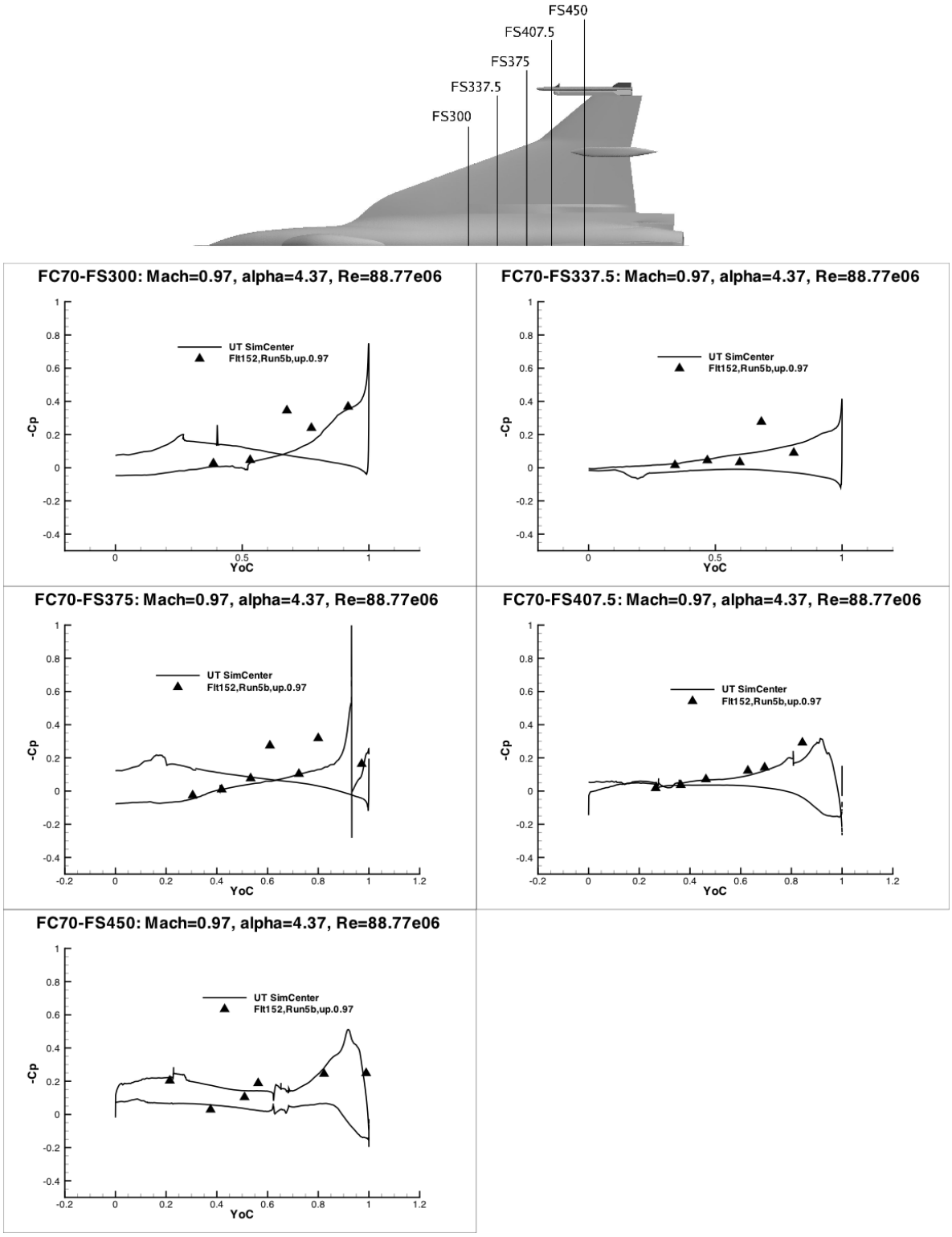

Figure 14-17: FC70 Surface Pressure Coefficient Comparisons for Axial Stations.

The first optional case is flight condition 25 (FC25), which is a subsonic Mach number at an angle of 19.84 degrees. The comparisons of the surface pressure coefficients are shown in Figure 14-18 and Figure 14-19. The computed solution agrees very well except at the last outboard *spa*n station. Since this is at a large angle of attack, it is reasonable to expect some unsteady flow. The last outboard station is close to the wing tip missile. Unsteady shedding of vortices from the missile is definitely possible. The integrated forces plotted versus iteration are shown in Figure 14-25. The X directed force seems to have leveled off, but the Y and Z directed forces are still oscillating after 8000 iterations. Unfortunately, the breakdown of forces on individual components of the aircraft was not computed, so it is hard to tell if the oscillations in the forces are emanating from the outboard location.

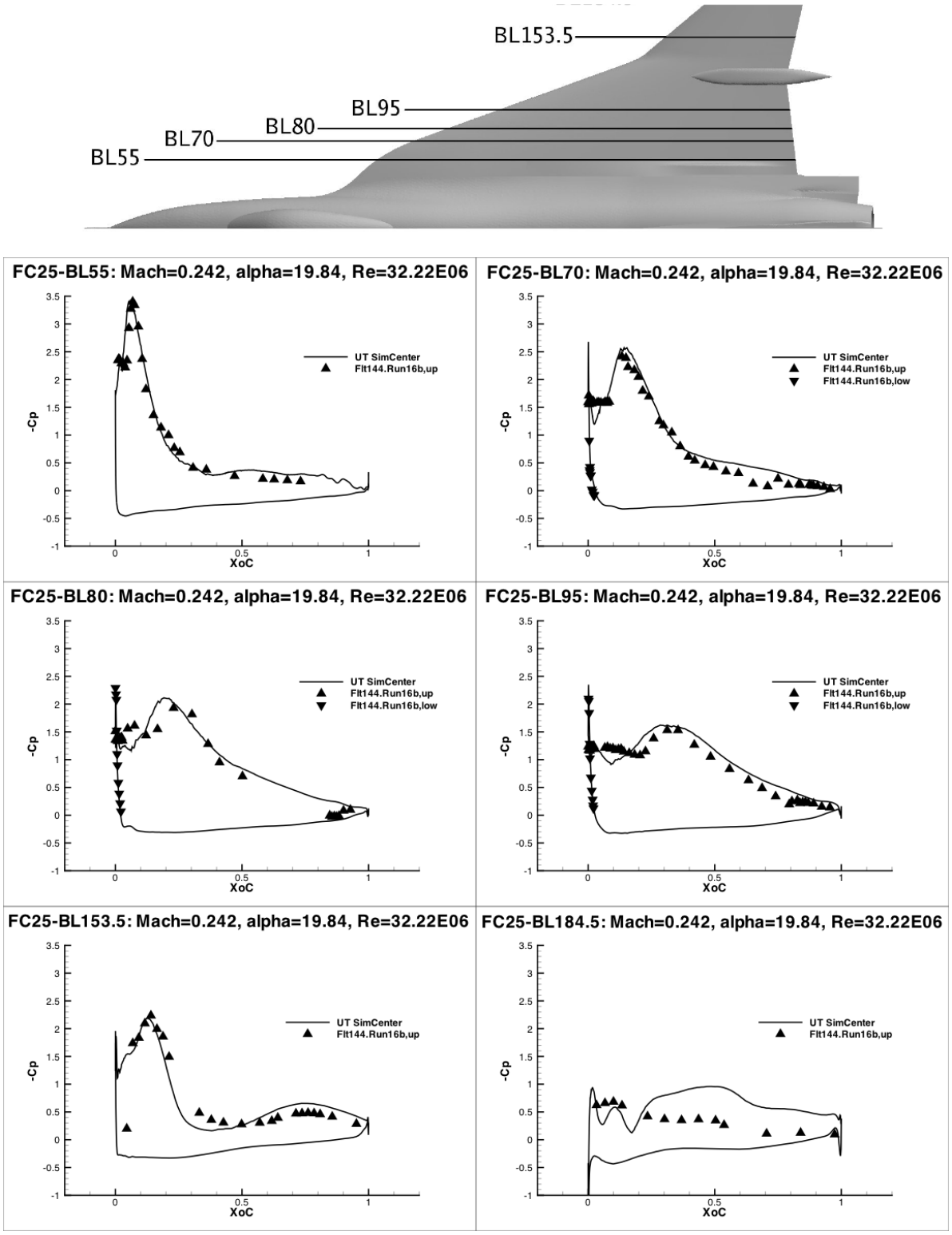

Figure 14-18: FC25 Surface Pressure Coefficient Comparisons for Span-Wise Stations.

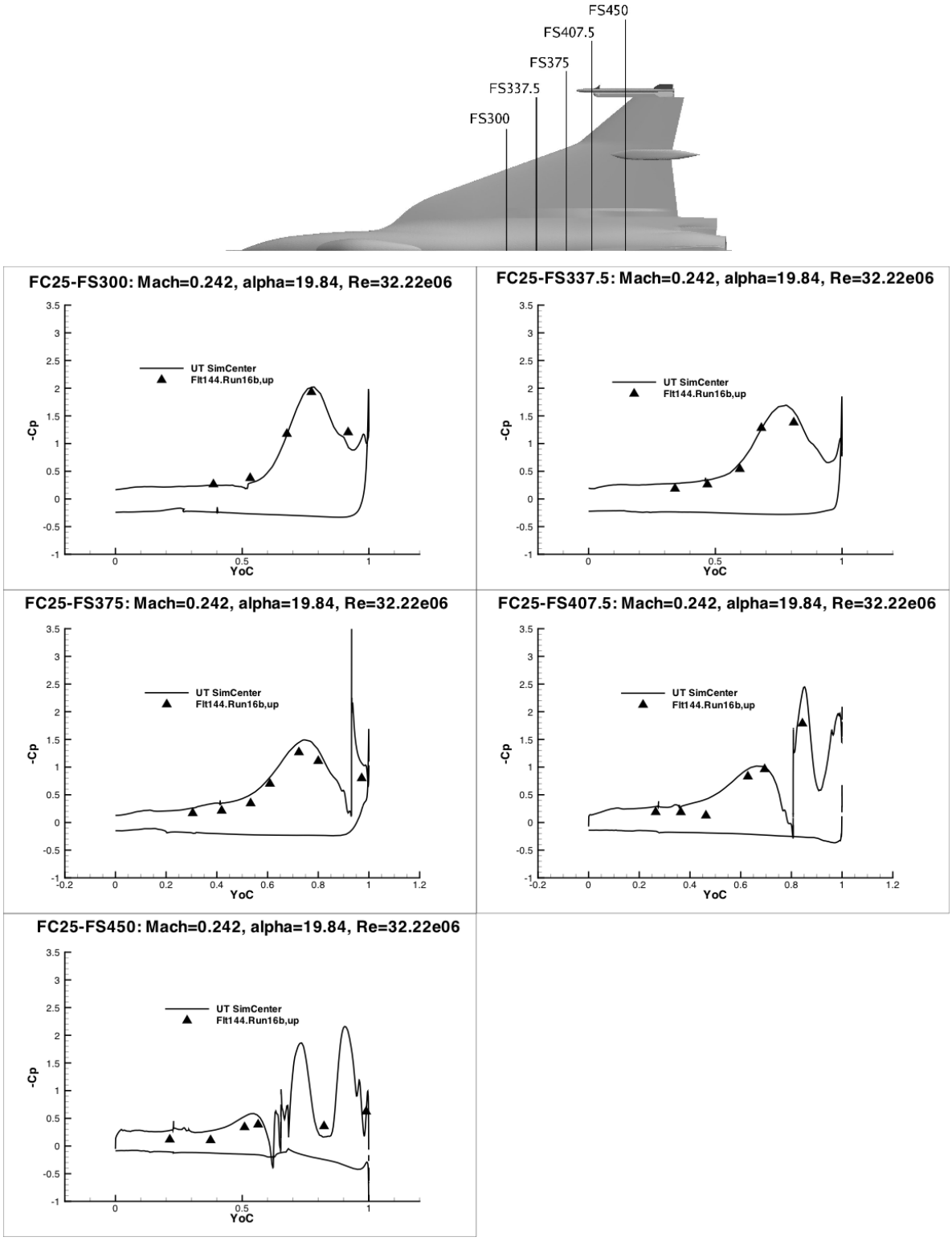

Figure 14-19: FC25 Surface Pressure Coefficient Comparisons for Axial Stations.

Flight condition 50 and 51 include positive and negative sideslip, respectively, so they require the use of a full span mesh. The half-span mesh used for all the previous cases was mirror-copied about the symmetry plane, creating a mesh with nearly 28 million points. These two cases were computed using 200 processors on a Linux cluster. Figure 14-20 and Figure 14-21 show the comparisons for flight condition 50, a positive sideslip of 5.31 degrees. The flight test data is listed as nominally +5 degrees. The computed results on the right side agree reasonably well with flight-test data. No flight test data was taken for the left side. Figure 14-22 and Figure 14-23 show the comparisons for flight condition 51, an input sideslip of -4.58 degrees.

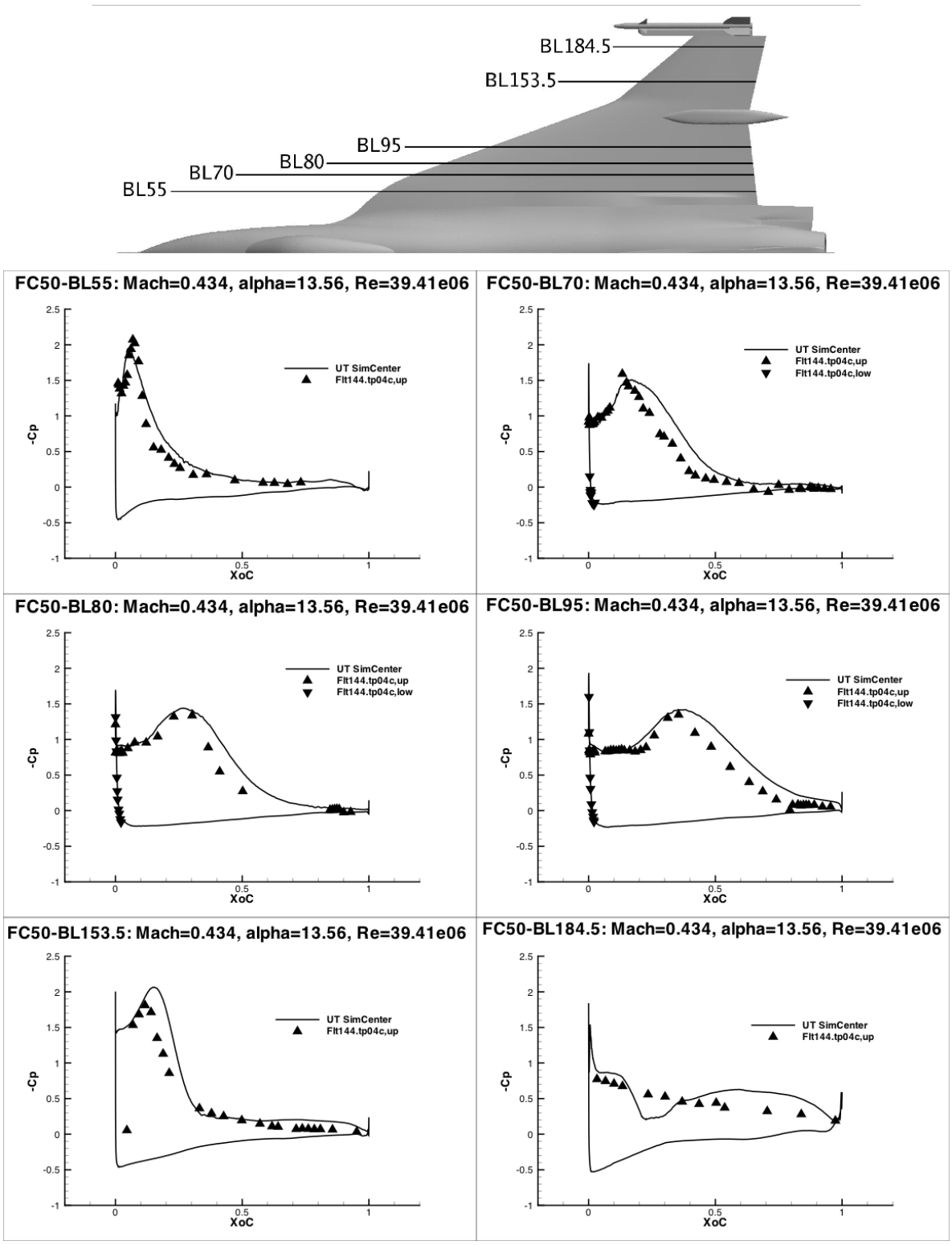

Figure 14-20: FC50 Surface Pressure Coefficient Comparisons for Span-Wise Stations.

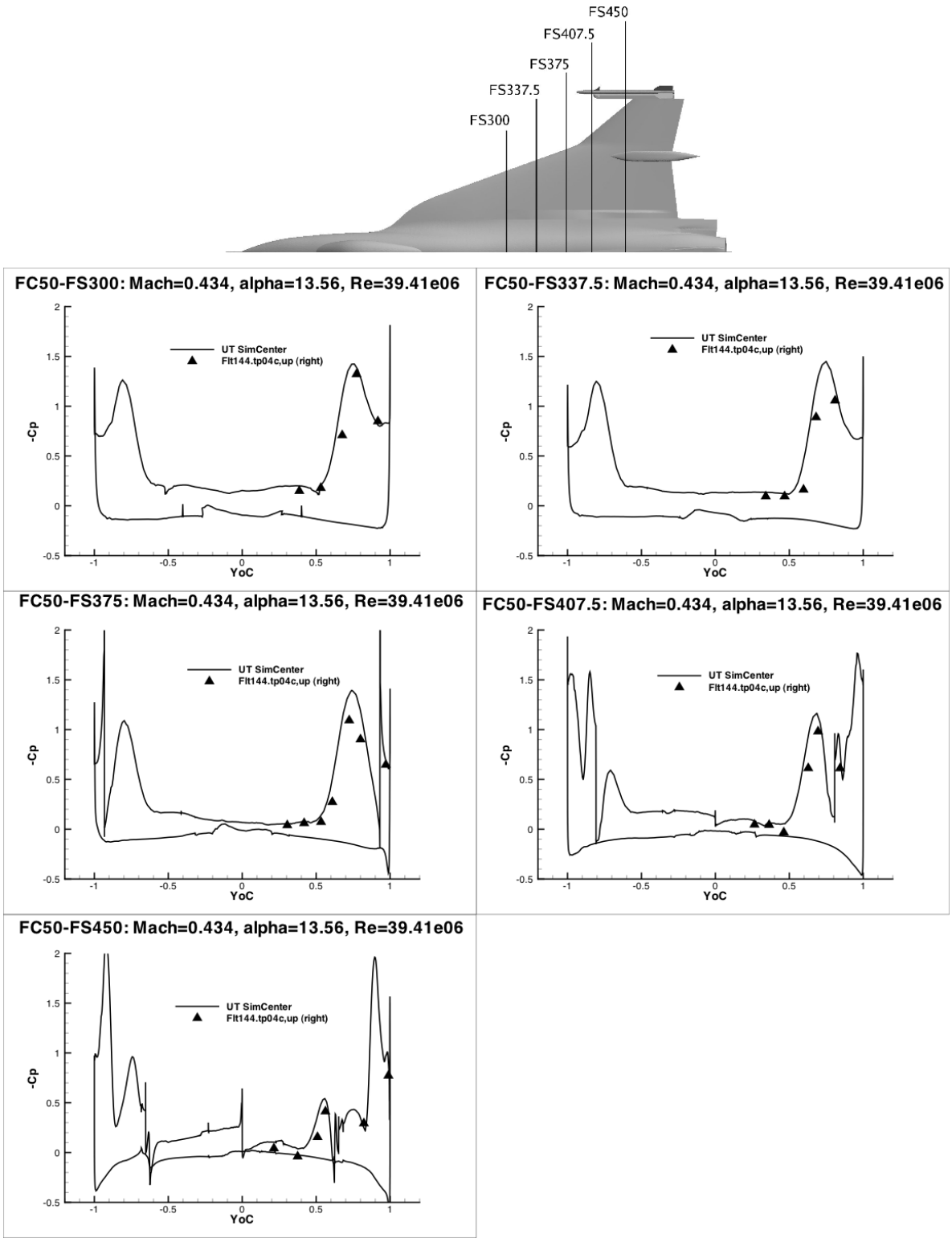

Figure 14-21: FC50 Surface Pressure Coefficient Comparisons for Axial Stations.

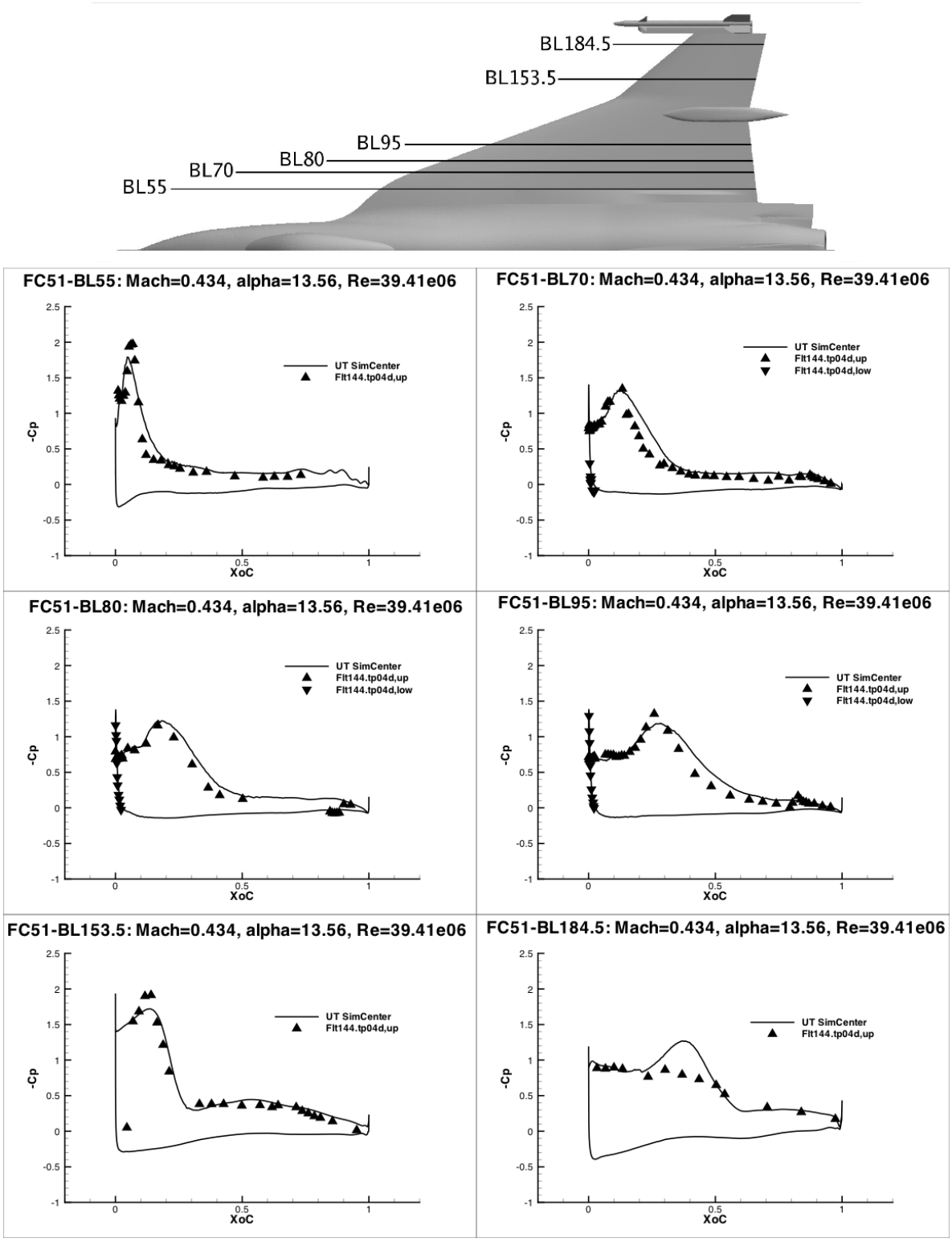

Figure 14-22: FC51 Surface Pressure Coefficient Comparisons for Span-Wise Stations.

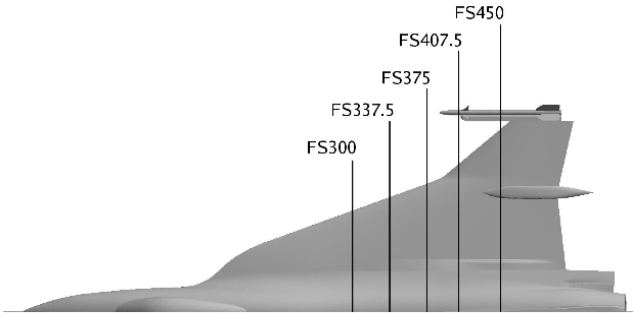

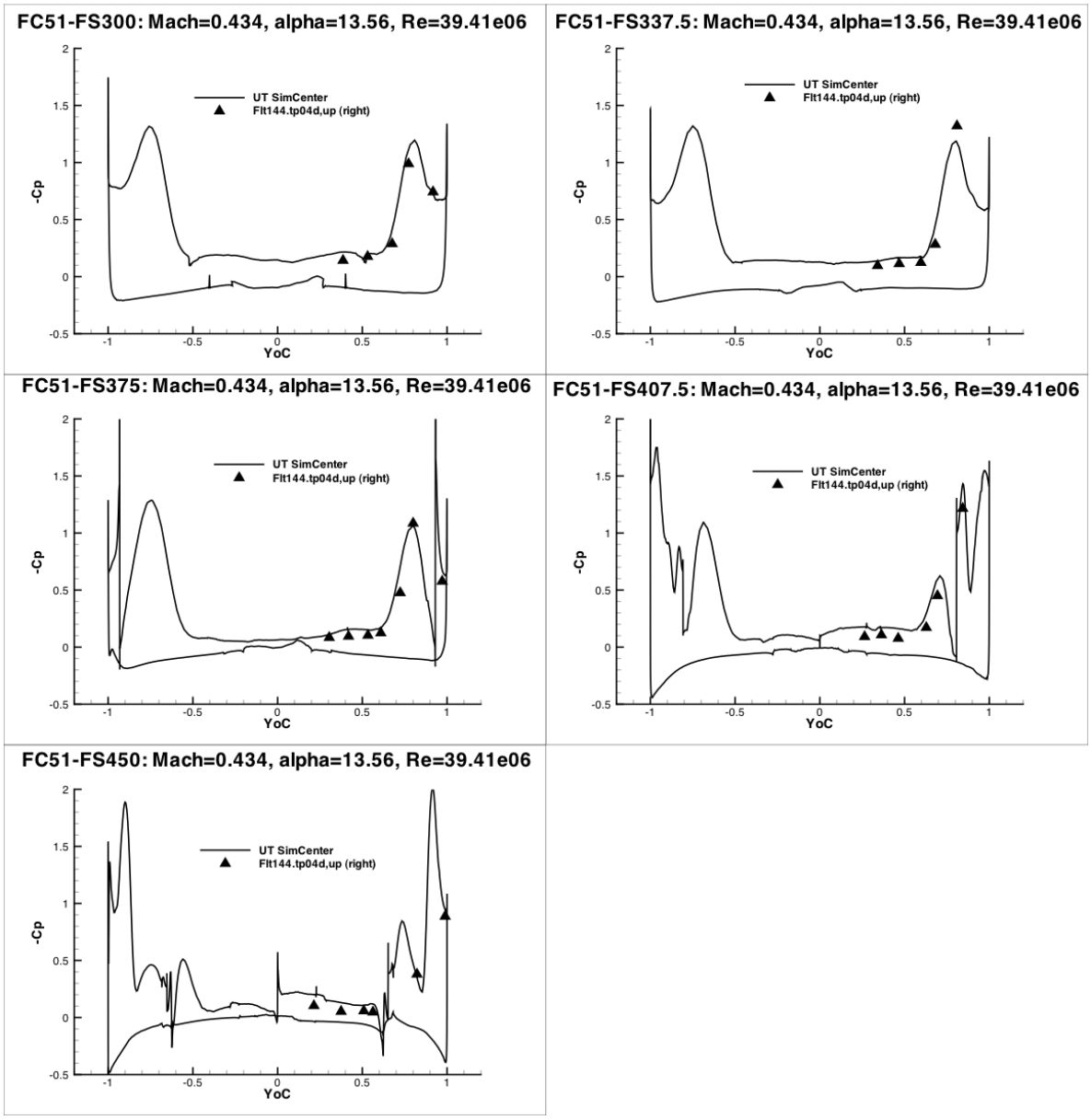

Figure 14-23: FC51 Surface Pressure Coefficient Comparisons for Axial Stations.

14.6.3 Selected Convergence Plots

Convergence histories for residual and integrated forces for selected cases are presented below. Only some of the cases are included to conserve space. The residual histories are shown to indicate the typical behavior seen with the use of the limiter. Figure 14-24 shows the residual history for case FC07. The flow solver was run with first order special accuracy for the first 2000 iterations. Then second order fluxes were used, but with a flux limiter. The residual exhibited an oscillatory behavior due to the flux limiter switching between first and second order accuracy. The main location where this switching took place was at the nozzle exit where the geometry was modeled with an aft facing base region. The flow attempts to accelerate around the sharp corner, but the limiter prevents overshoots and undershoots in flow variables by switching back to first order. The cell location where the switching takes place oscillates between mesh points. As a result of this oscillatory behavior, residual histories were not used to determine level of convergence of any of the cases.

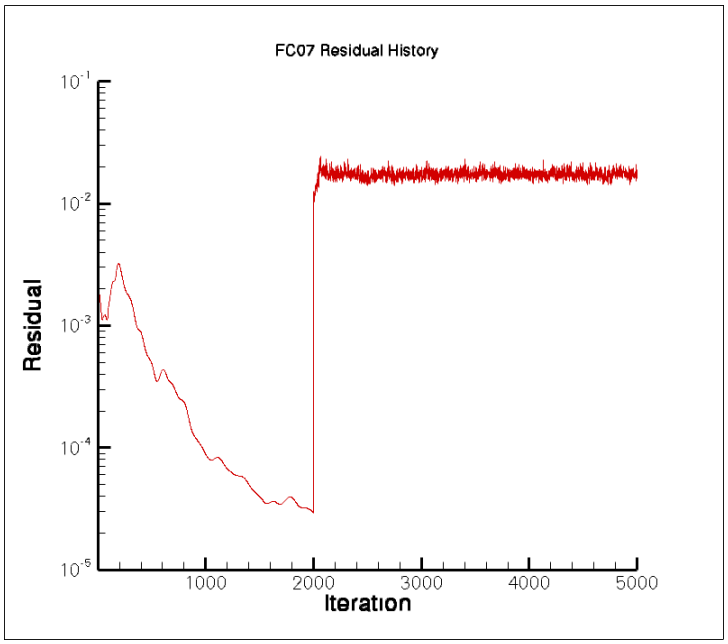

Figure 14-24: Residual History for Case FC07.

The force histories were used to track solution convergence. Most of the cases reached a steady state solution where all of the forces reached asymptotic values. Some cases exhibited an oscillatory behavior in one or more of the forces, indicating a tendency for unsteadiness in the solution. Figure 14-25 shows the oscillatory behavior in the Y & Z directed forces for case FC25, even after 8000 iterations. This is the high angle of attack case at subsonic speeds, so unsteadiness is reasonable. Judging from the pressure coefficient plots in Figure 14-18; the unsteadiness probably takes place at the outboard wing stations.

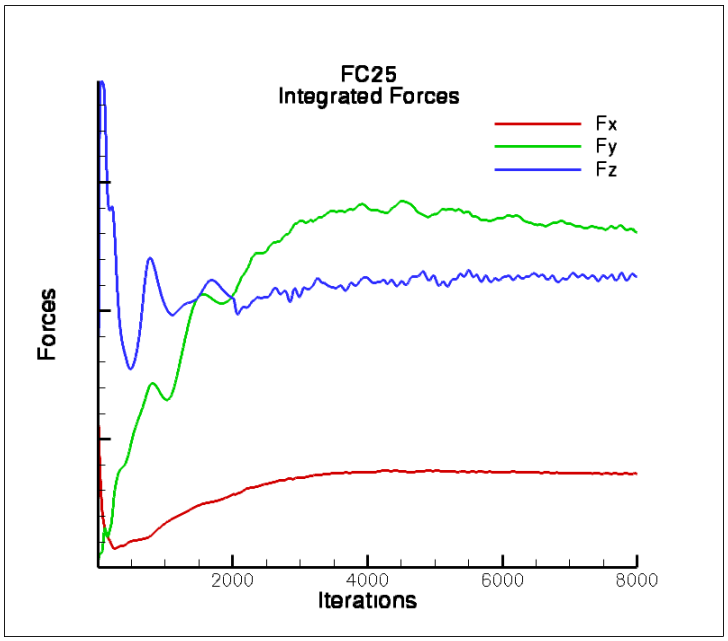

Figure 14-25: Integrated Forces Convergence History for Case FC25.

Other flight conditions did achieve a satisfactory level of convergence in the force histories. Figure 14-26 shows the convergence of the integrated forces for case FC51, a full configuration, sideslip case. The angle of attack is in the moderate range and the solution appears to be steady. All three forces show a steady behavior after 5000 iterations. Other flight conditions behaved in a similar manner.

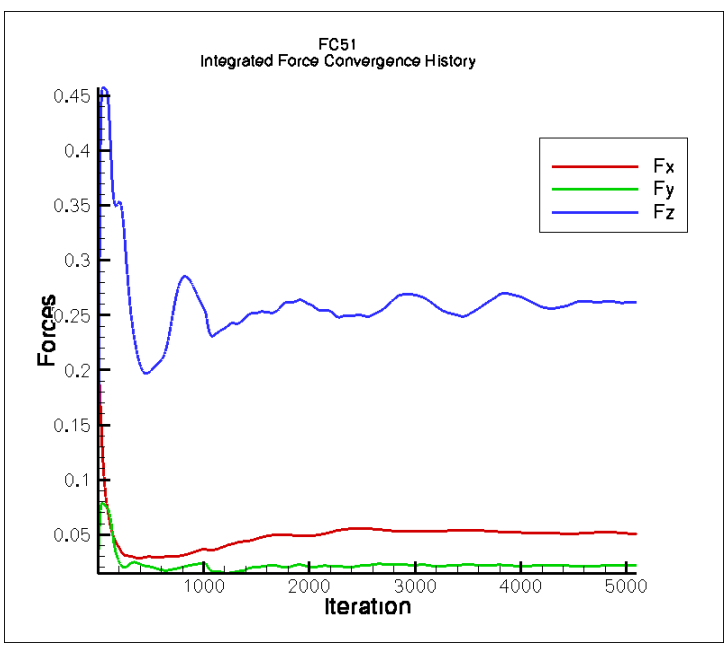

Figure 14-26: Integrated Forces Convergence History for Case FC51.

14.6.4 Field and Surface Color Contour Plots

Flowfield and surface color contours are shown in the next series of figures for selected flight conditions. Figure 14-27 shows color contours of pressure coefficient for flight condition FC07. This was a zero sideslip case that was computed using a half-span mesh. The solution was mirrored in the post-processing program, Fieldview, to make the plots [14-10]. Figure 14-28 shows color contours of vorticity magnitude for the same flight condition at various fuselage stations. Not all magnitudes of vorticity are shown; lower and higher values of vorticity magnitude are clipped from view.

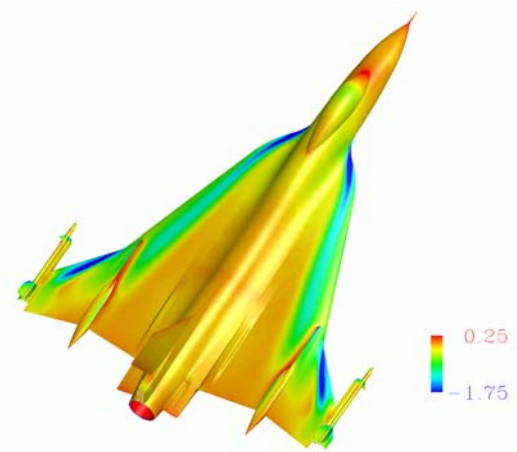

Figure 14-27: Surface Pressure Coefficient Color Contours for Case FC07.

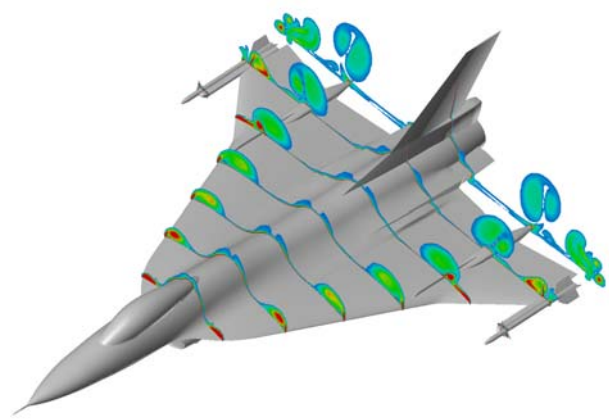

Figure 14-28: Axial Station Cuts of Contours of Vorticity Magnitude for Case FC07.

The same plots are made for case FC25, the high angle of attack case, in Figure 14-29 and Figure 14-30. The color contour levels are the same as shown in the figures for case FC07. The stronger vortices are evident in the deeper blue surface C_p contours and the larger regions of red and green in the vorticity magnitude plots. Both cases exhibit a strong vortex emanating from the leading edge of the wing. The primary vortex in case FC07 stays closer to the surface as it passes the airdam. The two red regions outboard of the airdam near the leading edge are counter-rotating vortices, one originating at the airdam and rotating outward and the other originating at the wing leading edge and rotating inward.

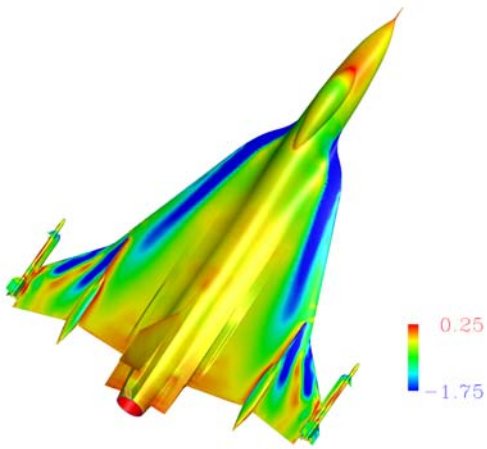

Figure 14-29: Surface Pressure Coefficient Color Contours for Case FC25.

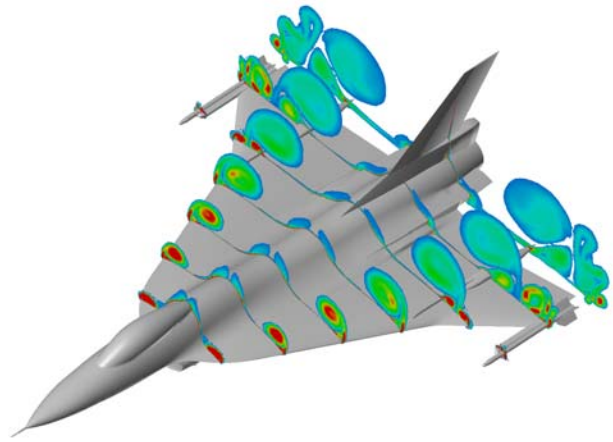

Figure 14-30: Axial Station Cuts of Contours of Vorticity Magnitude for Case FC25.

Case FC70 is the transonic case at a small angle of attack. A plot of the sonic surface is shown in Figure 14-31. The region inside this surface is supersonic flow. This demonstrates the complicated system of shocks and acceleration as the air flows over the top surface of the aircraft. The shock diamond pattern emanating from the nozzle is also visible.

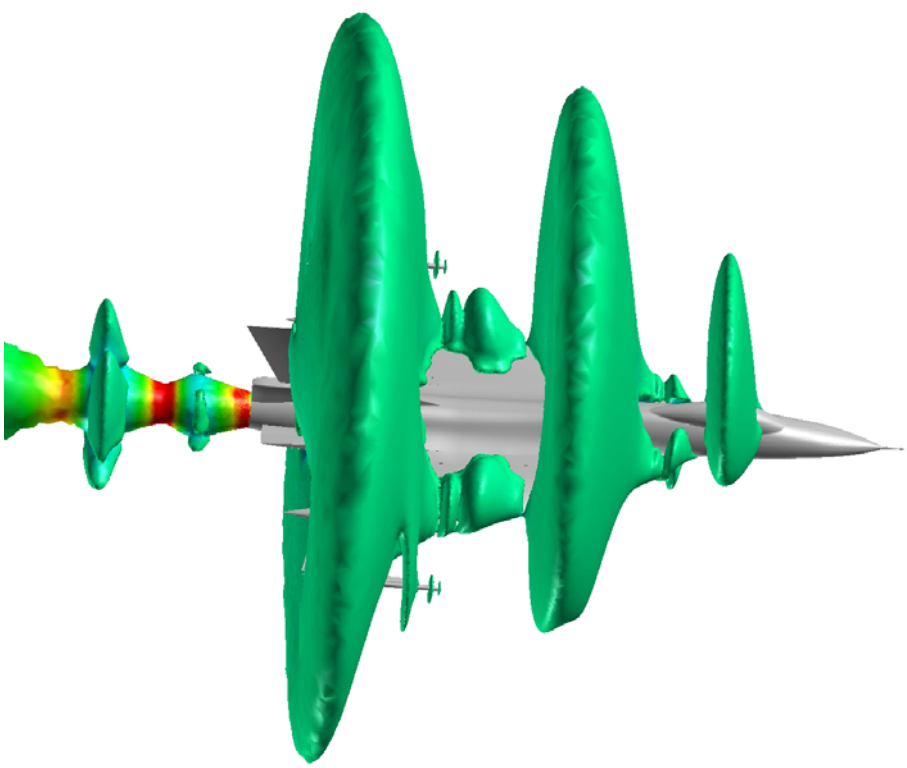

Figure 14-31: Case FC70 Sonic Surface Colored by Pressure.

Figure 14-32 shows the surface pressure coefficient color contours for cases FC50 and FC51. These are the two sideslip cases, so the full span mesh was used to compute the solutions. The color contour levels are the same for both images. FC50 had a positive sideslip angle of 5.31 degrees. The freestream vector impacts the aircraft from the right side. The paths of the leading edge vortices are shifted toward the left side of the aircraft, as shown in the top portion of the figure. FC51 had a negative sideslip angle of 4.58 degrees. The freestream vector impacts the left side of the aircraft, so the leading edges vortices are shifted toward the right side of the aircraft, shown in the bottom portion of the figure.

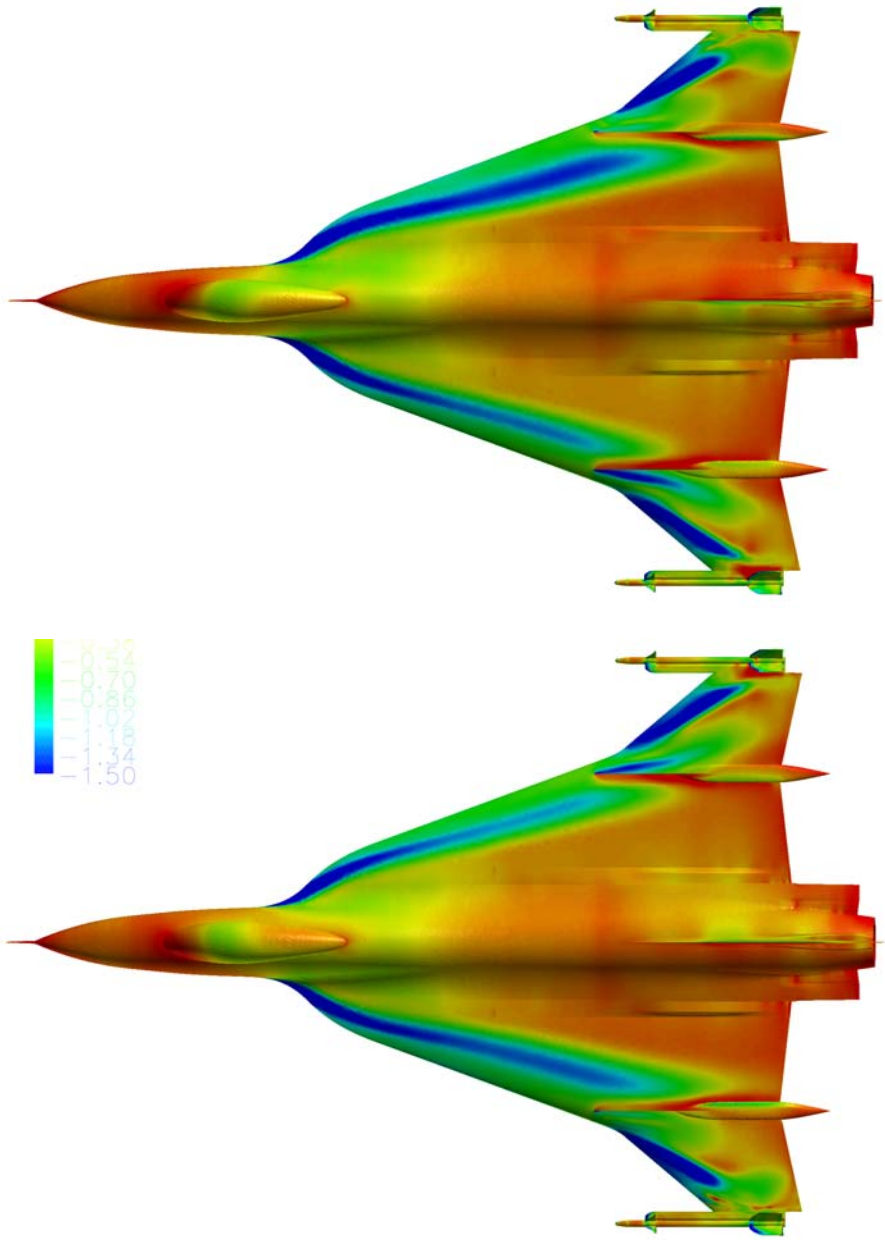

Figure 14-32: Surface Pressure Coefficient Contours for FC50 (top) and FC51 (bottom) with Color Range for C_p Values from -1.5 to 0.1.

The path of the vortices is readily apparent in Figure 14-33. This plot shows color contours of vorticity at the axial stations where the experimental data was taken. These contours include the negative and positive magnitudes. From this view perspective negative values are counter-clockwise rotating vortices and positive values are clockwise rotating vortices. Also include in the plot are streamlines showing the paths of the vortices. These streamlines were generated in Fieldview by releasing particles at selected locations on the vorticity contours and allowed to flow forward and backward. The streamlines are colored by the local static pressure, blue being low pressure and read being high pressure. The sideslip angle is evident in the path the streamlines take approaching the leading edge of the wing and travel over the top side of the fuselage, as they cross from the right side of the aircraft to the left side.

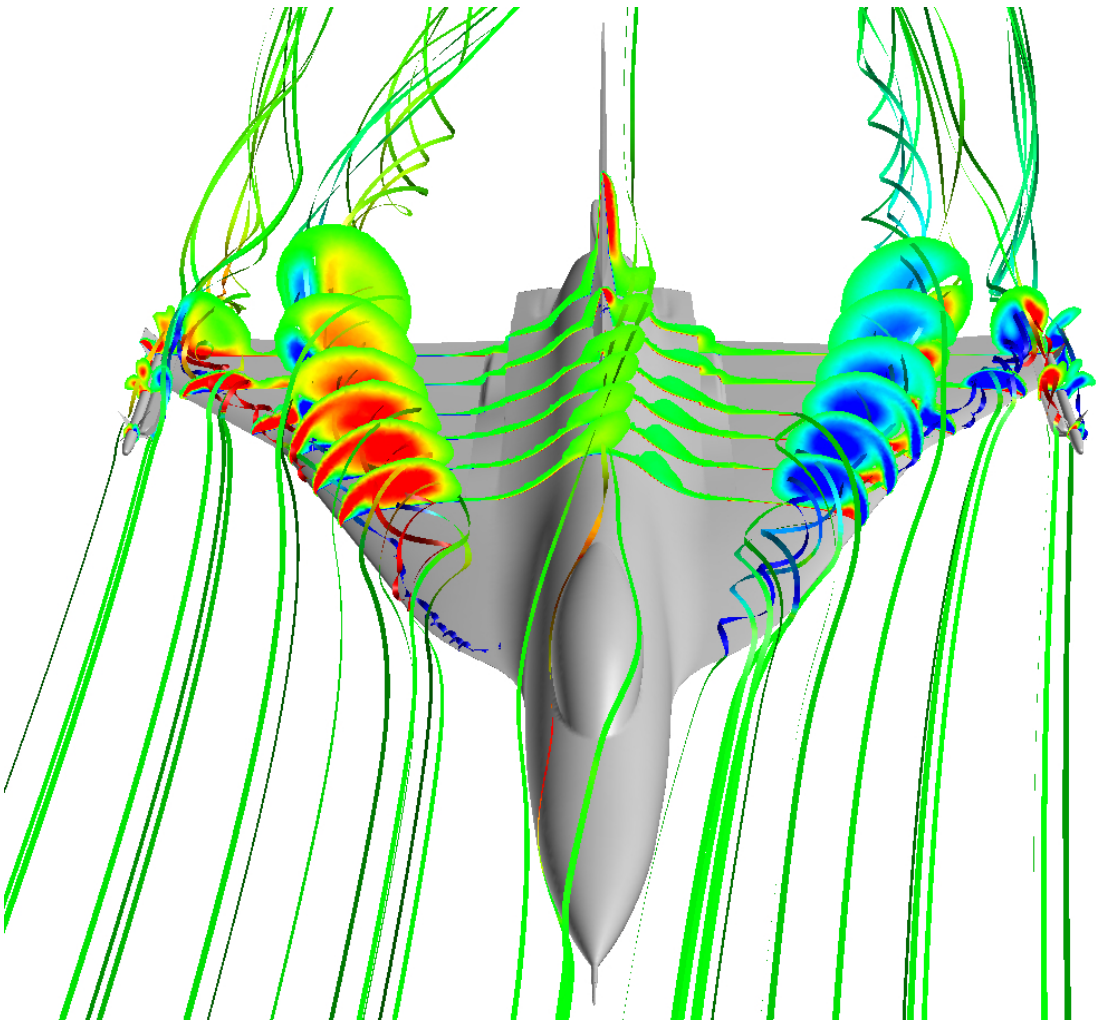

Figure 14-33: Axial Cuts of Vorticity Contours with Streamlines Tracking the Vortices for Case FC50.

14.7 CONCLUDING REMARKS

Seven viscous solutions for a F-16XL configuration were computed using the CFD tools at the UT SimCenter at Chattanooga as part of the NATO Technical Team AVT-113. The purpose of the NATO team was to determine

the readiness level for CFD solver to analyze highly vortical viscous flowfields. Viscous meshes for the analyzes were created using two different mesh generation packages. Inviscid meshes were generated using a commercial grid generation package call Gridgen. Viscous layers were added to this mesh using a mesh generation package developed at the SimCenter.

Initial solutions revealed grid resolution issues capturing the vortex path at the outboard span stations. A turbulence model study was performed to determine if the discrepancies were due to modeling issues. No improvement was observed based on turbulence modeling options. Finally, a manual refinement of the mesh was performed based on the known trajectory of the leading edge vortex at the outboard stations. The adapted mesh showed dramatic improvement in the solution accuracy at these span stations. All solutions were recomputed using the adapted mesh.

The computed solutions on the adapted mesh were compared to available flight test data, supplied to the team by NASA. Four of the computed cases were required of each team member. Three other cases were optional. Surface pressure plots showed reasonable agreement with the supplied flight test data for virtually all cases. Discrepancy between the computed surface pressure coefficients and the flight test data typically occurred near the wing tip; more so for the higher angle of attack than for the low to moderate angles of attack. The one transonic flight condition (FC70) showed the worst agreement with the flight test data. Comparisons at two of the six span stations for this case showed good agreement. One span station was near the wing root and the other was close to mid-span. One possible contributor to the discrepancy could be geometry modeling issues. The actual flight test for this case included significant leading and trailing edge flap deflections. No flap deflection was modeled in the CFD mesh. The computed vortex trajectories and strengths agreed well with the flight test data. The locations were generally accurate. The magnitudes of the suction peaks were slightly low in some cases and in agreement in other cases. Primary and secondary vortices were captured in the computed solutions.

Mesh resolution is critically important in accurately computing viscous vortical flowfields. The manual adaptation is evidence of that. A formal grid refinement study was not performed during this study, due to the required size of the full aircraft viscous mesh. This computer resource restriction is typical in cases of this size and complexity. An alternative to a formal grid refinement study might be to perform solution-based mesh adaptation. This can include mesh redistribution techniques as well as mesh refinement techniques.

14.8 REFERENCES

[14-1] Lamar, J.E., Obara, C.J., Fisher, B.D. and Fisher, D.F.: *Flight, Wind-Tunnel, and Computational Fluid Dynamics Comparison for Cranked Arrow Wing (F-16XL) at Subsonic and Transonic Speeds*, NASA TP-2001-210629, NASA Langley Research Center, February 2001.

[14-2] Pointwise, Inc., Gridgen User Manual, Version 15, http://www.pointwise.com/.

[14-3] Karman, S.L. Jr.: *Unstructured Viscous Layer Insertion Using Linear-Elastic Smoothing*, AIAA Journal, Volume 45, No. 1, pp 168-190, January 2007.

[14-4] Anderson, W.K.: *Grid Generation and Flow Solution Method for the Euler Equations on Unstructured Grids*, Tech. Rep. L-16986, NASA Langley Research Center, Hampton, VA 23665-5225, 1992.

[14-5] Anderson, W.K. and Bonhaus, D.L.: *An Implicit Upwind Algorithm for Computing Turbulent Flows on Unstructured Grids*, Computers in Fluids, Vol. 23, No. 1, pp. 1-21, 1994.

[14-6] Anderson, W.K., Rausch, R.D. and Bonhaus, D.L.: *Implicit/Multigrid Algorithms for Incompressible Turbulent Flows on Unstructured Grids*, AIAA Paper 95-1740, 1995.

[14-7] Pankajakshan, R., Remotigue, M.G., Taylor, L.K., Jiang, M., Briley, W.R. and Whitfield, D.L.: *Validation of Control-Surface Induced Submarine Maneuvering Simulations Using UNCLE*, 24th Symposium on Naval Hydrodynamics, Fukuoka, Japan, 2002.

[14-8] Hyams, D.G., Sreenivas, K., Sheng, C., Briley, W.R., Marcum, D.L. and Whitfield, D.L.: *An Investigation of Parallel Implicit Solution Algorithms for Incompressible Flows on Multielement Unstructured Topologies*, AIAA 2000-0271, 2000.

[14-9] Briley, W.R., Taylor, L.K. and Whitfield, D.L.: *High Resolution Viscous Flow Simulations at Arbitrary Mach Number*, Journal of Computational Physics, pp. 79-105, 2003.

[14-10] Intelligent Light, Inc., URL: http://www.ilight.com/.

[14-11] Tecplot, Inc., URL:http://www.tecplot.com/.